

1
2
3
4
5
6
7
8
9
10
11
12
13
14
15
16
17
18
19
20
21
22
23
24
25
26
27
28
29
30
31
32
33
34
35
36
37
38
39

Improved Analysis of STEVE Photographs

Charles L. Bennett¹ and Notanee Bourassa²

¹Retired from Lawrence Livermore National Laboratory, Livermore, CA, USA

²Saskatchewan Aurora Hunters, Saskatchewan, Canada

Corresponding author: Charles Bennett (Charlie_Bennett@comcast.net)

Key Points:

- A method for accurate registration and synchronization of digital photographs of STEVE is presented
- The nature of the flux producing STEVE emissions can be quantified from such photographs using a model for auroral precipitation
- It is found that the STEVE green picket fence and purple bands share magnetic field lines

Abstract

We present a new approach for the analysis of high-resolution digital camera photographs taken by photographers who have fortuitously been able to capture rare events such as the glowing sky phenomenon known as STEVE. This method is especially effective with a time lapse series of images of the night sky taken under constant camera settings with a steady pointing. Stars, planets and satellites seen in such images can be used to determine precise and accurate registration of camera pixels to coordinates of angular altitude and azimuth. The location of satellites in the image enables precise and accurate synchronization of the images. We apply these techniques to the series of photographs of STEVE taken on 25 July 2016. We confirm the altitude structure previously found for STEVE. We find it most likely that the green picket fence features often seen during STEVE events are produced by auroral electron precipitation. With the precipitation assumption, we are able to extract novel information about the energy spectrum of the particles responsible for the production of STEVE luminosity in this particular event. Similar analyses of archived digital photographs may constitute a treasure trove of important data for improved understanding of rare and transient events such as STEVE.

Plain Language Summary

Extremely rare events are sometimes captured in photographs by people who just happen to be in the right place and at the right time to notice something unusual happening in the night sky. Modern digital cameras can have such high pixel counts and such high sensitivity that these lucky photographs can contain valuable information about the rare events that is not available from any other source. The location of stars, planets and even occasional satellites in these images can be used to precisely interpret the timing and location of the events captured in the pictures. The methods described and computer software included in this paper can be used to make such analysis easier. The mysterious phenomenon known as STEVE is one example of such a rare event, and provides an example of how these techniques can work.

40

1 Introduction

41 The nighttime optical phenomenon STEVE was originally noticed and named by a
42 network of enthusiastic auroral photographers. The initial publication in the scientific literature
43 discussing this phenomenon by (MacDonald E. N.-L., 2018, doi:10.1126/sciadv.aag0030),
44 observed the correlation between Steve and subauroral ion drift (SAID) and created the
45 backronym “Strong Thermal Emission Velocity Enhancement” (STEVE). A typical STEVE
46 event appears as a narrow purple band of predominantly east-west oriented light, located
47 equatorward of concurrent auroral activity and may extend from horizon to horizon. Sometimes,
48 in addition to the purple band, intermittent green streaks, known as the “picket fence” are also
49 seen. The question as to whether STEVE is produced by particle precipitation or ionospheric
50 skyglow was raised very early by (Gallardo-Lacourt, 2018, doi:10.1029/2018GL078509), and
51 still remains a topic of debate.

52 In (Archer, 2019, doi:10.1029/2019GL084473; Chu, 2019, doi:10.1029/2019GL082789),
53 the vertical distribution of the optical emissions from a STEVE event on 16 September 2016 was
54 determined. In this event the green picket fence structures were aligned with the geomagnetic
55 field and extended from 95- to 150-km. The purple band of STEVE extended between 130- and
56 270-km and was found to extend vertically along similar magnetic field lines to the picket fence
57 features.

58 Spectroscopic observations by (Gillies, 2019, doi:10.1029/2019GL083272) of a 10 April
59 2018 STEVE event found the green picket fence structure to be associated with strong OI (557.7
60 nm) emission. In contrast, the purple band was found to have a spectrum very similar to the
61 ambient airglow, and approximately equal in intensity, thus locally doubling the airglow along
62 the brightest portions of the purple band. This is most clearly seen in their figure 1 by a
63 comparison of the spectrum of STEVE with neighboring background pixels slightly poleward
64 and equatorward. In (Nishimura, 2019, doi:10.1029/2019GL082460) it is suggested that electron
65 precipitation could be a possible driver of the green picket fence features, if not the purple band
66 structures. On the other hand, based on the presence of 5577 Å OI emission and near absence of
67 N_2^+ first negative emission in one particular STEVE event (Mende, 2019,
68 doi:10.1029/2019GLO86145) claim that this constitutes strong evidence against the hypothesis
69 of precipitation.

70 Many of the scientific studies of Steve have exploited photographs taken by auroral
71 photographers in conjunction with the more accurately calibrated network of All-Sky-Imager
72 (ASI) photographs and satellite observations. Although these auroral photographers may
73 sometimes be scientific professionals, quite often they are amateur photographers or auroral
74 enthusiasts that happen to be in the right place at the right time. By virtue of the fortuitous
75 proximity of the these photographers to the STEVE events they photographed, these photographs
76 have extraordinarily high spatial resolution and sensitivity compared to the better calibrated ASI
77 and space-based images, and we believe that they represent a significant reservoir of highly
78 detailed data that could be very helpful to improving our understanding of STEVE. The network
79 of “citizen scientists” organized by (MacDonald E. C., 2015, doi:10.1002/2015SW001214) is
80 particularly effective in this regard.

81 Here, we describe an improved method for the determination of the 3-d spatial structure
82 of STEVE and more accurate temporal synchronization of such photographs for use in
83 conjunction with ASI images and/or space-based data. We then apply this method to the 25 July

84 2016 event originally published by (MacDonald E. N.-L., 2018, doi:10.1126/sciadv.aaq0030).
85 Finally, we demonstrate how the energy distribution and temporal behavior of the particles
86 producing STEVE emissions may be extracted from such photographs. From the quality of the
87 fits of observed green light emission to models, we believe this analysis bolsters the case that the
88 green picket fence features of STEVE are produced by auroral electron precipitation.

89 Because the photographic data examined here doesn't have sufficient spectral
90 information to confirm or deny the presence of N_2^+ first negative emission in the 25 July 2016
91 STEVE event, it isn't clear whether the arguments against auroral electron precipitation in the 10
92 April 2018 STEVE event are relevant to our observations of the 25 July 2016 event.

93 2 Methodology

94 The 25 July 2016 STEVE event was photographed by N. Bourassa from a site near
95 Regina Saskatchewan (REGI) with a Nikon D810 digital camera. Most of these images were
96 taken with a sensitivity set to ISO 4000. The REGI RAW camera data was converted to 16-bit
97 digital numbers using Nikon's Capture NX-D version 1.5.3 software (Nikon, 2019) with no
98 adjustment applied to the colors. The readout noise of the D810 is approximately 3.8 electrons,
99 with a dark current of 0.25 e/pixel/s at 30° C according to (Lodriguss, 2020). As the Bourassa
100 photographs were taken with the camera exposed to the cool evening air, although the
101 temperature was not recorded, it was undoubtedly at a lower temperature than 30° C, and thus
102 the dark current is less than 1 e/pixel for the 4 s exposures discussed in this article. These readout
103 noise and dark current levels are relatively insignificant compared to the "clutter" noise of
104 intensity fluctuations due to faint stars, galaxies and other celestial objects that are present in the
105 Bourassa photographs.

106 Concurrent with these photographs published in (MacDonald E. N.-L., 2018,
107 doi:10.1126/sciadv.aaq0030), although data was stored from 10 distinct All Sky Imager (ASI)
108 sites, relatively clear sky conditions were only available from the 4 Canadian sites at Lucky Lake
109 (LUCK) in Saskatchewan, Athabasca (ATHA) in Alberta, Pinawa (PINA) and The Pas (TPAS)
110 in Manitoba. The complete sequence of images from the ASI cameras are available for download
111 from (University of Calgary, 2018). The details on the spatial resolution, spectral coverage and
112 site location for these various cameras are tabulated in Table 1. The ASI data can be converted to
113 absolute units of radiant intensity using a combination of a dark flat field and the sensitivity
114 Rayleigh per Digital Number (R per DN) values.

115 2.1 Synchronization Using Bright Satellite Transits

116 In order to accurately triangulate the location of objects seen concurrently from multiple
117 cameras, it is important to know both the location of each camera, and the time of each image. In
118 the case of the ASI cameras, the geodetic coordinates are included in the meta-data associated
119 with each image as well as a time stamp. On the other hand, the high-resolution images of
120 STEVE sometimes available from fortuitous observations by auroral photographers do not
121 always have such high accuracy location or time stamps. In the 25 July 2016 STEVE event
122 examined here, the REGI site location is well remembered by N. Bourassa, and is clearly
123 identifiable in some of the photographs, but we have found that the time stamp was off by 165
124 seconds. Although this error may be insignificant for the analysis of relatively slowly changing
125 structures, the green picket fence features seen in STEVE are especially dynamic, and accurate
126 time synchronization is important. For example, in the later REGI images taken at a 2 s cadence

127 with 1 s exposure, there are significant motions and changes observable in the green picket fence
128 “posts” from frame to frame. The first step in our method for accurate triangulation of structures
129 between various sets of images is accurate correction of the time stamps associated with each
130 image.

131 The orbits of bright low-earth orbit (LEO) satellites can be calculated with great accuracy
132 (Aida, 2013) using Twoline Elements (TLEs) that are publicly available from (Kelso, 2019). As
133 an example, the absolute location of the International Space Station (ISS) can be determined to
134 within a few km at any given time. As the ISS is particularly bright, an accurate synchronization
135 of the registered time stamps for each of the ASI cameras can be accurately and precisely
136 determined using the observed meridian crossing times of the ISS in the data from each camera.
137 The clock offset times found in this way that are required to synchronize the 4 ASIs to the ISS
138 are listed in **table 1**. The small ASI clock offset times quantify the accuracy of the current
139 synchronization technique assuming there is no error in the official ASI time stamps.

140 2.2 Registration Using Bright Stars

141 Once an accurate synchronization of the image times is in hand, pixels in each image are
142 registered to local angular coordinates of azimuth and elevation using a number of stars in the
143 images. The Right Ascension (RA), Declination (DEC) and magnitude values are taken from the
144 Yale bright star catalog (Hoffleit, 2014). Using the time and geodetic location of the camera for
145 any given photograph, the RA and DEC for all stars in the bright star catalog are converted to
146 local angular coordinates using the starCat2Obs function from (Crouse, 2017). This function
147 includes corrections for parallax and atmospheric refraction and enables the use of celestial
148 objects observed even near the horizon. A set of clearly identified stars, as well as planets when
149 apparent in the data, are chosen using the Matlab cselect function. To aid this process, all stars
150 brighter than a specified magnitude limit are plotted as circles with radii proportional to
151 brightness, and the locations seen in the observed data are compared with the predicted locations
152 of the bright stars. Non-linear least squares fitting determines an estimate of the parameters for
153 the observed camera that converts pixel coordinates in the photograph to azimuth and altitude.
154 For the REGI camera a primarily gnomonic projection (Weisstein, 2019) was used. For the ASI
155 cameras with fisheye lenses, a primarily linear equidistant projection (Bettonvil, 2005) was used.
156 For both types of lenses, correction for barrel distortion was required to provide acceptable
157 registration. The Matlab (Mathworks, 2019) functions used for these fits and image registrations,
158 with the explicit definition of the fitting parameters listed in **table 1**, are available in the
159 supplemental materials. For each of the four ASI cameras the fit parameters were found to be
160 valid for the full series of images. For the REGI images, a number of different camera
161 orientations were used over the series of photographs, but within any given stable pointing, a
162 single registration was valid. The REGI registration parameters for six different camera
163 orientations are tabulated in **Table 1**.

164 Note that the rms fit error for the REGI data represents approximately one arcminute of
165 error in angular position. Without the correction in the present analysis for atmospheric
166 refraction effects (~ 30 arcminutes near the horizon) the fit error for stars or planets near the
167 horizon would be much greater than one arcminute. Since stars at the celestial equator appear to
168 move one arcminute in only four seconds, this illustrates the importance of accurate
169 determination of the times of the photographs. At the other extreme of quality, the 20-fold larger

170 fit error for the PINA data is due to the lower sensitivity and much poorer seeing conditions at
171 this site that allowed the use of only a small number of reference stars.

172 It can be seen from a comparison of the magnitude limit of approximately 11 in all three
173 spectral channels for the digital camera images to the magnitude limit of only 3 or 4 for ASI
174 cameras (even with co-adding of 10 or 20 frames) that the digital camera images have far
175 superior sensitivity. It can be seen from the order of magnitude smaller error (in unit circle
176 terms) of the digital camera images that the spatial resolution is also far superior to the ASI
177 images. These sensitivity and resolution advantages make modern digital camera data taken by
178 observers that fortuitously happen to be in the right place at the right time potentially extremely
179 useful, especially with regard to analysis of the sort displayed in **figures 5** and **6** below.

180

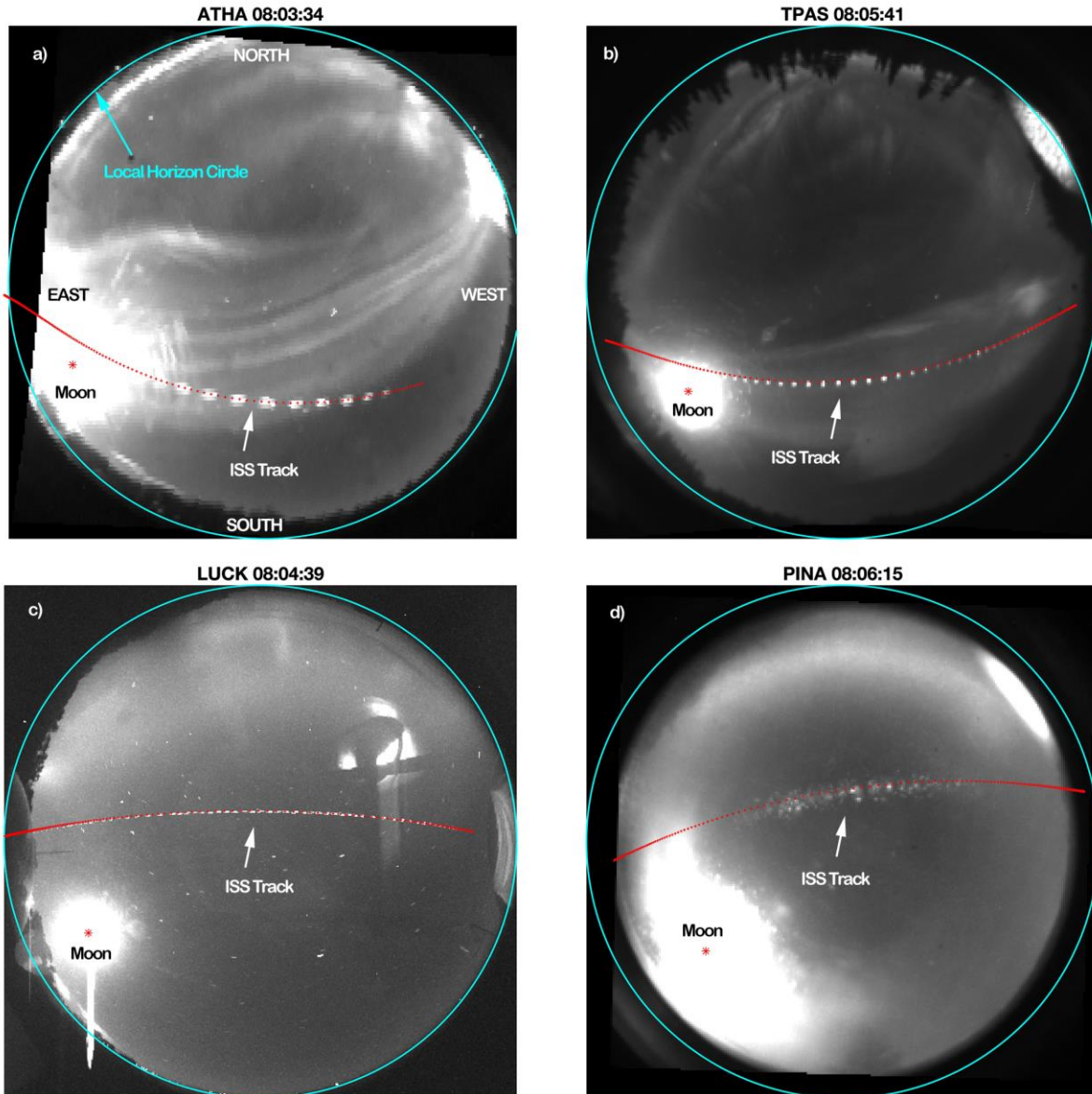
181 Table 1

182 *Image Registration Parameters*

Site Designator:	REGI	LUCK	ATHA	TPAS	PINA
Location	Regina, Saskatchewan	Lucky Lake, Saskatchewan	Athabasca, Alberta	The Pas, Manitoba	Pinawa, Manitoba
Site Latitude (°N)	50.688	51.154	54.603	53.994	50.163
Site Longitude (°W)	104.501	107.264	113.644	100.941	96.066
Site Altitude (m)	659	709	693	236	247
Spectral Coverage	RGB	630±2 nm	CYGM	Monochrome	Monochrome
Fit Type	Gnomonic	Fisheye	Fisheye	Fisheye	Fisheye
Fit Epoch (UTC)	5:59:13	05:00:14	06:08:01	5:05:29	4:44:49
Clock Offset Needed (s)	-165	-2	-1	-2	-1
ISS Meridian Crossing	8:04:49.9	8:04:22.4	8:03:18.6	8:05:25.5	8:06:14.8
Barrel Distortion	Quadratic	Linear	Linear	Linear	None
Gnomonic lamda0(rad) or Fisheye X0(unit circ)	-0.5668	-0.0133	-0.1137	.0157	-0.0385
Gnomonic phi0(rad) or Fisheye Y0(unit circ)	0.9905	0.0202	-0.0216	.0306	0.0145
Scale	0.8311	0.9955	0.9298	.9337	.9243
Theta0(radians)	3.0708	0.0520	-0.0900	0.0113	-0.0314
Bradial or Bx	2.6163	1.206	-0.0558	-0.3935	9.016
By	1.7994		0.0434	0.2533	
Bxx	1.8692		7.616	9.1947	
Byy	1.8747		6.5599	4.7683	
Bxy	0.1375		-0.0011	0.6465	
rms error (pixels)	1.91	0.55	0.32	0.72	0.72
rms error (unit circle)	0.00023	0.0026	0.0039	0.0055	0.0057
Pixel Resolution	4912x7360	512x512	128x256	256x256	256x256
No. of Frames coadded	1	10	10	10	20
Total Exposure (s)	4	20	50	10	20
No. of Points Fit	71	89	38	48	32
No. of Parameters	9	5	9	9	5
Red Magnitude Limit	11.2				
Green Mag. Limit	11.3				
Blue Mag. Limit	10.8				
Grayscale Mag. Limit		3.5 (10 frames)	3.5 (10 frames)	4 (10 frames)	3 (20 frames)
Other REGI Epochs	6:07:18	6:07:26	6:07:32	6:07:46	6:07:53
Gnomonic lamda0(rad)	2.7122	-0.4427	5.5526	-0.6672	-0.3761
Gnomonic phi0(rad)	2.6925	0.8511	1.3252	1.9898	2.4390
Scale	0.8311	0.8312	0.8315	0.8292	0.8287
Theta0(radians)	0.0347	3.1746	2.9196	-0.2262	-0.0450
Bx	1.8953	-1.9047	-1.2762	1.351	1.796
By	-2.8018	2.6374	2.8724	-2.9598	-2.879
Bxx	1.8215	1.8194	1.8613	1.8969	1.9219
Byy	1.7561	1.6856	1.5784	1.6415	1.7590
Bxy	-0.1915	-0.2223	-0.1588	-0.1225	-0.0554
rms error (pixels)	1.24	1.79	1.39	1.63	1.78
rms error (unit circle)	0.00021	0.00029	0.00021	0.00020	0.00022
No. of Points Fit	50	66	80	81	63

183

184 **Table 1.** The image registration parameters for each of the sites discussed in the text are
185 tabulated here. The site designator four letter acronyms for each site are in row one, followed by
186 information on the locations in the next four rows. The spectral coverage for the camera systems
187 at each site are then listed. The type of fit involved in the registration process is listed, and the
188 epoch used to generate the expected locations of the stars and planets for use in determining the
189 control points for the registration process. The clock offset needed for bringing the recorded time
190 stamps from each sites' set of data into synchronization with the time of the meridian crossing of
191 the International Space Station (ISS) is then listed, together with the meridian crossing time
192 computed from the ISS orbital elements. The nature of the correction for camera lens barrel
193 distortion, either linear or quadratic is listed. The next several rows contain the best fit
194 parameters found to bring the positions of the chosen set of control points into best agreement
195 with their correct values at the fit epoch. The details of the functions of the registration are
196 included in the supplemental materials. At the end of the list of fit parameters, the quality of fit in
197 terms of the rms error between control points and known values is given both in terms of pixel
198 units and in terms of the "unit circle", in which the local horizon is at unit radius. The format of
199 the images is given in pixels. The number of sequential frames of data coadded in order to
200 improve the signal to noise ratio of the data is listed, followed by the number of points used in
201 the fit. The number of parameters for each fit is listed, followed by a quantification of the
202 magnitude of stars that are detectable in the image, either in terms of the separate colors for the
203 REGI case, or in terms of the grayscale level for the other images. The last 13 rows contain the
204 same information for the five different camera orientations used in the panoramic sweep at the
205 times listed.



206
 207
 208
 209
 210
 211
 212
 213
 214
 215
 216
 217
 218

Figure 1. For the ATHA, TPAS, LUCK and PINA ASI imagers, a Maxima Merged “MM” composite image (described further in the text) from a number of camera frames nearest the local meridian crossing time of the ISS is shown. The ISS location in the ASI imagers computed from its orbital elements is indicated by a series of red dots corresponding to the ISS location at three second intervals. The three s interval chosen represents the cadence of the LUCK and TPAS cameras. Each image’s title time is chosen to be the frame time closest to the meridian crossing of the ISS over the respective ground station. The frame time for each ASI corresponds to the time at the end of each camera’s exposure. In these MM composite images, the ISS shows up as a bright “dashed line” in each image, with the dash length proportional to the exposure time for each ASI frame (five s for ATHA, two s for LUCK and one s for both TPAS & PINA). With perfect synchronization, the leading end of each “dash” should line up with a red dot.

219 2.3 Check of registration accuracy using “Maxima Merging” technique

220 A check of the end-to-end accuracy of the process of time synchronization and image
221 registration is shown in **figure 1**. In this figure, the ASI label and UTC at the time of the ISS
222 meridian crossing over each imager are used as titles for each image. The location of the local
223 horizon is indicated by the large cyan circle. Each photograph is oriented with NORTH at the top
224 and WEST to the right, as explicitly indicated on the ATHA image. Computed ISS locations at 3
225 second intervals, starting at 8:01:47 (the time that the ISS is first illuminated on this particular
226 orbit by the sun) and ending at 8:09:41 (the time that the ISS reaches the cyan horizon in the
227 LUCK image) are shown by the red dots in **figure 1**. Here, for each of the 4 ASI’s, the series of
228 registered images nearest the closest time to the meridian crossing for each camera are combined
229 by “Maxima Merging” (MM) and shown. For every pixel in such an MM image, the maximum
230 intensity value from the series of images being merged is used. As a result, for moving objects,
231 such as the International Space Station, a series of streaks are seen. The length of each individual
232 streak is a function of the exposure time of the camera, the speed of the moving object, the
233 distance to the moving object, and the location of the moving object. It can be seen that the
234 exposure times of each of the 4 ASI cameras is consistent with the length of the streaks in each
235 merged image. The number of separate images merged is greatest for the LUCK case, as the ISS
236 is observed for the longest time interval (342 seconds) at this location. The motion of some stars
237 over the 342 second interval in the merged image is also apparent. For the LUCK MM image,
238 near the center of the image, every frame of LUCK data is merged and clearly separated
239 “dashes” are apparent and can be seen to line up well with the location of the ISS red dots.
240 Further from the center of the LUCK MM image, where the ISS observations become more
241 crowded, either every other, or every 4th LUCK image was merged in order to verify the timing
242 of the ISS observed positions by having clearly separated “dashes”. A similar sub-selection of
243 images is used for the ATHA and TPAS contributions to the MM image, in order to clearly
244 associate ISS positions with the observed “dashes”, except that because of the inherently poorer
245 resolution of the ATHA, TPAS and PINA data, even near the center of the image, only every
246 other frame is merged. In the PINA image shown, it was clearly raining at the time of the ISS
247 crossing, the sky was quite cloudy, and the individual ISS images are quite blurry.

248 The quality of the agreement between the ISS image locations computed purely from the
249 satellite orbital elements and the observed locations in the *registered* ASI images provides an
250 overall validation of the current approach both to the registration of ASI images using stars and
251 planets as well as to the synchronization of images taken from widely spaced cameras that are
252 viewing the same rapidly moving object. This is particularly important for the analysis of
253 dynamic structures, such as the purple bands, and especially the green picket fence posts of
254 STEVE.

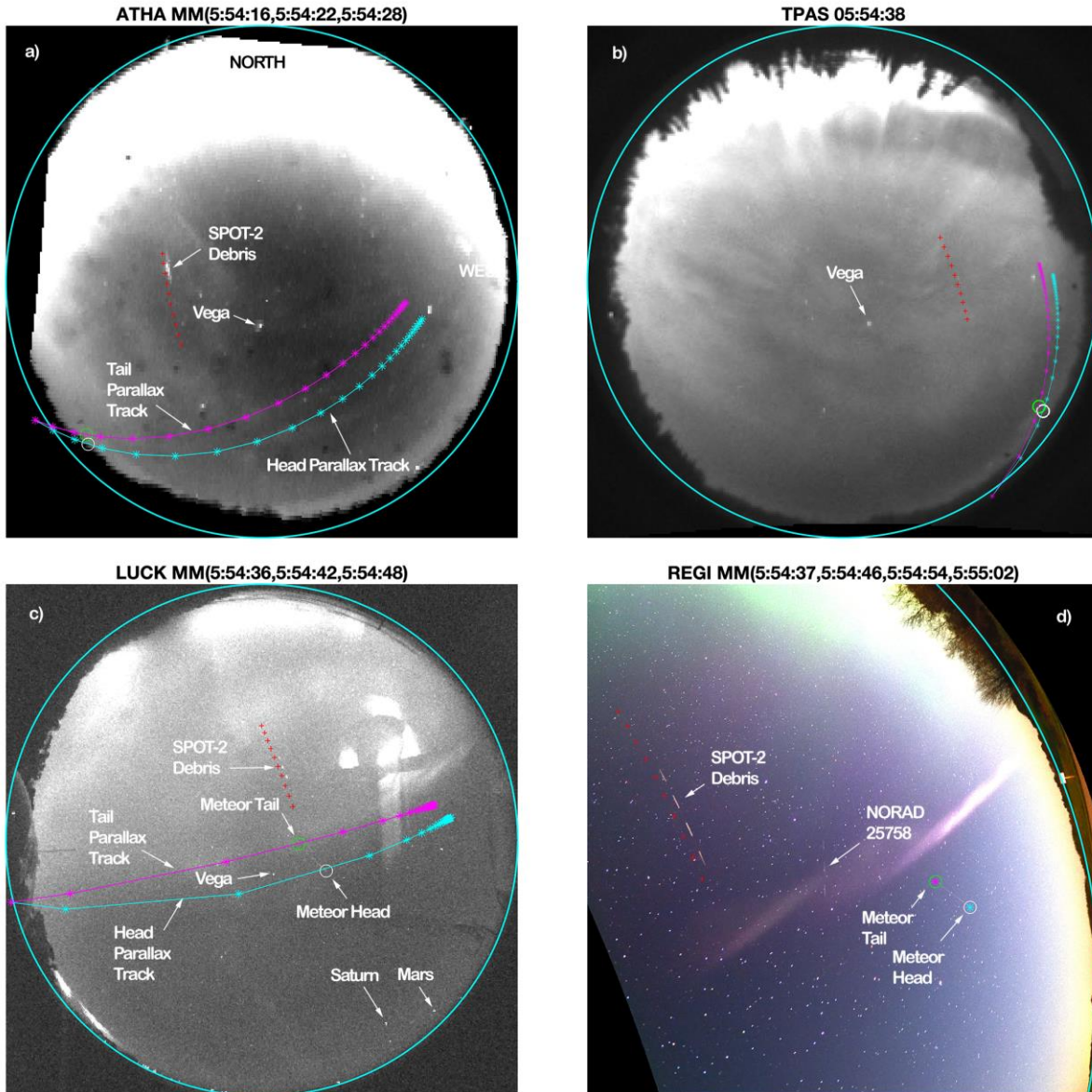
255 Although the ISS was not captured in any of the REGI images, another bright satellite
256 seen in all the ASI cameras (except for PINA because of cloud cover) is NORAD-20436, which
257 is a bit of residual debris from the SPOT-2 satellite (de-orbited in July 2009). This satellite is
258 also seen in REGI and this allows for the synchronization of its photographs.

259 In **figure 2**, the SPOT-2 debris streaks are indicated, as well as the NORAD-25758
260 satellite and a meteor. The meteor was captured by both the LUCK and REGI cameras and
261 provides an additional and independent confirmation of the quality of the registration as well as
262 the quality of the synchronization. The REGI image shown has four successive photographs
263 merged, as described above for the ASI images in **figure 1**, for the four brightest appearances of
264 the SPOT-2 debris from the REGI perspective. In the case of colored images, the maxima for

265 each color are merged separately. The meteor streak appears in only the 5:54:37 REGI image.
266 The LUCK image shown has three photos (at times indicated in parentheses) merged,
267 corresponding to the brightest appearances in LUCK. The meteor streak appears only in the
268 5:54:36 LUCK exposure. Similarly, the ATHA image has three bright appearances from the
269 ATHA perspective merged. Only the single TPAS 5:54:38 photo is used, as the cloud cover
270 obscured much of the sky at this time. Superimposed on all four images are a series of red dots,
271 corresponding to the computed position of the SPOT-2 debris at six second intervals from
272 5:54:13 to 5:55:07. Note that the brightness of the SPOT-2 debris exhibits a “flare event” during
273 its passage and varies rapidly as it happens to reflect sunlight towards the different ground
274 stations at differing times. It is found that the error between the computed satellite positions and
275 the observations are in disagreement by approximately 15 km in both the cross track and along-
276 track directions at an altitude of approximately 640 km. It is plausible that the TLEs for this
277 defunct satellite are not as accurate as the TLEs for the ISS, and for this reason, the discrepancy
278 between the predicted and observed track is greater. Considering both the possible TLE errors
279 for the SPOT-2 satellite, as well as timing errors associated with “flaring”, the estimated error in
280 the value of the clock offset for REGI using the SPOT satellite debris alone may be more than a
281 few seconds. Ignoring these possible systematic errors, the SPOT debris data leads to an
282 estimated clock offset for REGI of -165 seconds.

283 2.4 Parallax Track Analysis of 3-dimensional Geometry

284 Based on the SPOT-2 debris-based synchronization of REGI to LUCK, the 5:54:37 REGI
285 exposure, having a duration of four seconds, ended one second after the 5:54:36 LUCK exposure
286 of duration two seconds. The exposure of the 5:54:36 LUCK image shown would therefore fall
287 entirely within the exposure time of the 5:54:37 REGI image. As a result, the precisely
288 determined locations for the head and tail of the meteor seen in these images can be used to
289 determine the altitude distribution along the track of the meteor using a “parallax track” analysis
290 method. This method is based on triangulation of corresponding objects seen in simultaneous
291 photographs from multiple locations but has the advantage of simplifying the location and
292 identification of objects seen in multiple photographs.



293
 294 **Figure 2.** Various images used in the synchronization of the REGI photographs to the ASI
 295 photographs are shown here. In **a)** a “Maxima merged” MM composite of ATHA images at the 3
 296 times indicated in the title, in **b)** a single TPAS frame, in **c)** an MM composite of LUCK
 297 images at the three indicated times, and in **d)** an MM composite of REGI images at the four indicated
 298 times. Moving objects having significant luminosity for a longer duration that the individual
 299 camera exposures appear as “dashed lines” in the MM composites. In each image, the computed
 300 locations of the SPOT-2 satellite debris at six s intervals are marked with red dots. Moving
 301 objects having significant luminosity for a shorter duration than the individual camera exposures
 302 appear as single “streaks”. The meteor seen in a single LUCK and a single REGI frame provides
 303 such an example.
 304

305 A particular point of interest, such as that marked by the magenta asterisk in the REGI
 306 image at the tail of the meteor, corresponds to specific azimuthal and elevation angles from the
 307 REGI point of view. This particular point will appear somewhere along a curve in the other

308 imagers, with the location determined by the altitude of the point. Representative locations,
309 spaced at 100 km intervals along the line of sight extending from the camera at the REGI site in
310 the direction corresponding to the magenta asterisk in the REGI image, are indicated by the
311 magenta asterisks shown superimposed on the images from the other imagers. These are labeled
312 “Parallax Tracks”. The magenta asterisks in each image are joined by magenta line segments.
313 The altitude of the magenta asterisk point in the REGI image corresponding to the tail of the
314 meteor is determined by the intersection of the magenta parallax track with the observed location
315 of the meteor tail in the LUCK image indicated by the green circle.

316 Similarly, the cyan asterisks linked by cyan line segments represent the line of sight
317 corresponding to the center of the white circle indicating the location of the meteor head in the
318 REGI image. Just as for the magenta case, the altitude of the cyan asterisk in the REGI image is
319 determined by the intersection of the cyan parallax track with the center of the white circle
320 indicating the head of the meteor as seen in the LUCK imager. Parallax tracks are quite helpful
321 in the process of altitude determination but for clarity are not shown in later figures.

322 Since the meteor trail extends the full distance between the parallax tracks superimposed
323 on the LUCK image, it is verified that the meteor light occurred entirely within the two s LUCK
324 camera exposure, and that the LUCK exposure happened entirely within the four s REGI
325 exposure. This allows a lower bound of 18 km/s to be placed on the meteor speed. This speed is
326 well within the normal range of meteoric speeds (Hankey, 2019) of 11 km/s to 72 km/s. The
327 head and tail altitudes, approximately 100 km and 130 km respectively, are also quite reasonable
328 meteoric values. Finally, it can be concluded from the meteor track alone, that the relative clock
329 offsets between REGI and LUCK are accurate to \pm one second.

330 In the REGI image shown in **figure 2**, in addition to STEVE and the green auroral
331 activity, the pair of LEO satellites and the meteor are all simultaneously visible, with an
332 enormously large range of altitudes. The common auroral analysis approach of mapping ASI
333 data to a single altitude is inadequate for the analysis of such images. In contrast, the approach
334 described here involving the use of “parallax tracks” works quite well, provided clear points of
335 interest can be identified in nearly simultaneous images taken from at least two sites at different
336 locations. A parallax track is especially helpful for the location and identification of an object at
337 an unknown altitude in a crowded field. It can be seen, for example, that the meteor was so near
338 the horizon relative to both ATHA and TPAS, that it would naturally not be expected to be easily
339 detectable in those images.

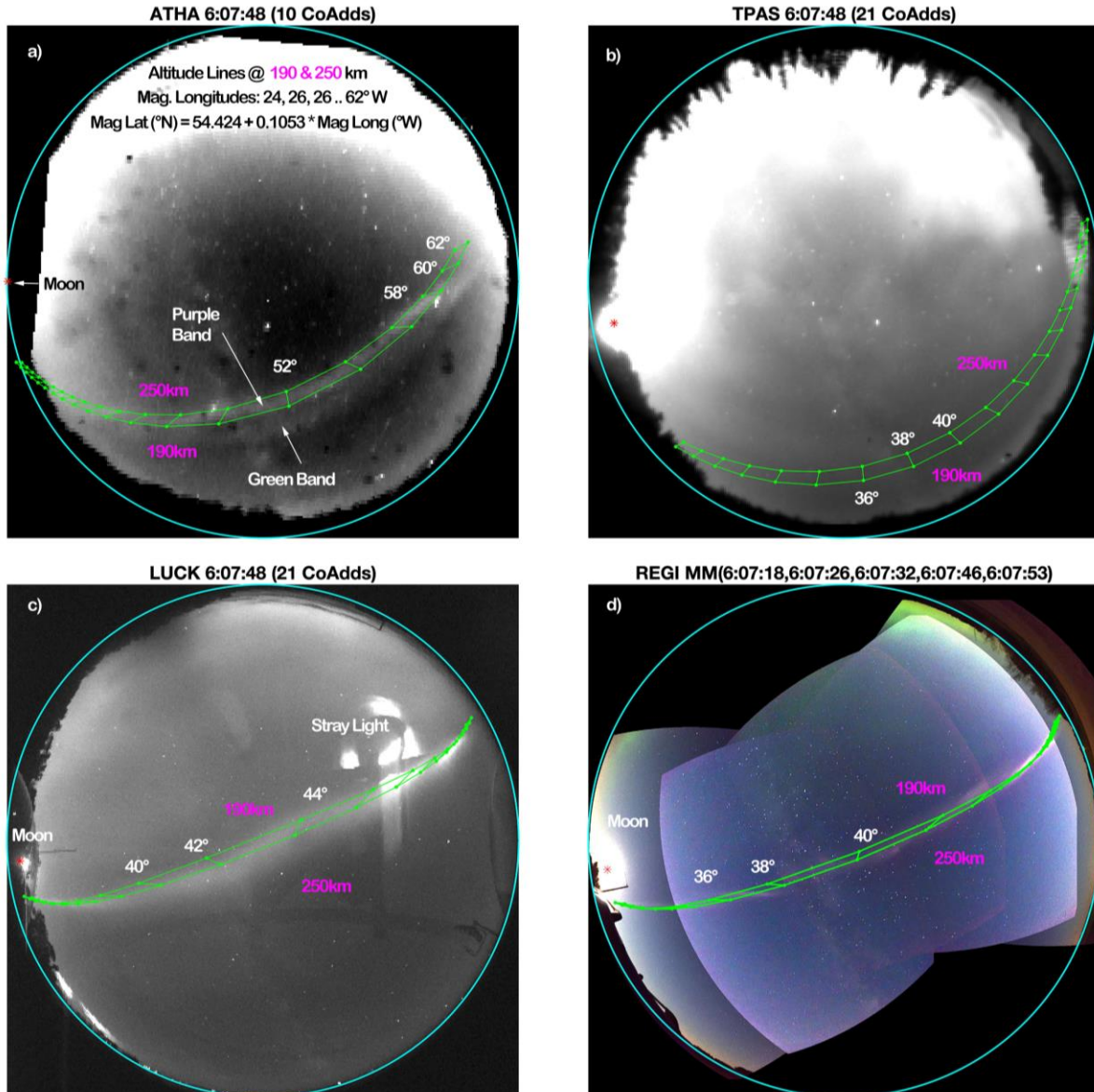
340 2.5 Synthetic All-Sky Image Creation from Panoramic Sweep

341 **Figure 3** displays data from a time that a “panoramic” sweep of five photographs was
342 taken across the night sky from the REGI site. These exposures were made sequentially from
343 West to East. The details of these five exposures are listed in the last 13 rows in **table 1**. Because
344 the registration errors for these images are so small (the rms error is approximately one
345 arcminute) the MM REGI image effectively produces a synthetic ASI image. In regions of the
346 sky not covered by a given component image, intensity values of zero are used, so such images
347 do not contribute to the MM composite. Intensity and color variation artifacts are noticeable near
348 the edges of some of the sub-images. These edge artifacts are the result of a slight vignette effect
349 from the camera lens. These edge artifacts do not affect the location of features in the composite
350 image. In order to reduce saturation in the MM image, the component images at both horizons
351 were scaled by 50%. In order to cover approximately the same time interval represented in the
352 REGI composite image, as well as to reduce noise, 21 LUCK frames, 21 TPAS frames and 10

353 ATHA frames were coadded rather than combined by MM. The time labels indicate the mean
354 time of the coadded images.

355 Superimposed on the LUCK, ATHA, TPAS and REGI images is a grid of magnetic field
356 line vertices joined by line segments shown in green. The magnetic field was computed using the
357 Enhanced Magnetic Model (EMM) Matlab code from (Crouse, 2017). This EMM model uses an
358 order 720 spherical harmonic expansion (Maus, 2010, doi: 10.1029/2010GC003026) to represent
359 the earth's magnetic field. The values of the magnetic field computed with this model were
360 compared with the entire day's series of 86,400 SWARM satellite measurements. The maximum
361 difference in direction between the EMM calculated field and the SWARM measured field over
362 the entire day was 0.93° and the largest differences were seen as the satellite passed through
363 regions of auroral activity. In the subauroral vicinity of the STEVE overpass shown in
364 (MacDonald E. N.-L., 2018, doi:10.1126/sciadv.aag0030) the maximum difference between the
365 EMM model and the SWARM measured field in direction was only 0.06° and this angular
366 difference *changed* by only 0.02° as STEVE was crossed. The magnetic field line passing
367 through any particular point in space can be traced up or down in space by following the local
368 direction of the EMM magnetic field and can be uniquely identified by the Centered Dipole (CD)
369 coordinates of magnetic latitude and longitude of the "foot of the field line" where such a tracing
370 reaches the nearest zero altitude location with respect to geodetic coordinates.

371 The series of magnetic field line vertices shown lie at altitudes of 190 and 250 km. They
372 are shown at intervals of 2° in magnetic longitude from 24° to 62° West, as indicated by the
373 white labels next to some of the magnetic longitude lines. Note that the higher altitude 250 km
374 grid lines lie to the north of the 190 km grid lines from the ATHA and TPAS perspectives, but to
375 the south from the REGI and LUCK perspectives.



376
 377 **Figure 3.** Co-added ASI images from ATHA, TPAS and LUCK at 6:07:48 are shown in a), b)
 378 and c) respectively. In d) is shown a synthetic All-Sky image created from the “Maxima
 379 Merged” composite of five REGI photographs from the times indicated in the heading. A grid of
 380 vertices linked by line segments at altitudes of 190 and 250 km for coordinates at 2° steps in
 381 magnetic longitude, with latitudes following the linear relation shown in a) is shown in green
 382 superimposed on all images. Selected longitudes are indicated in white numerals on each image.
 383 The band of STEVE luminosity clearly visible in LUCK and REGI closely follows the green
 384 grid. In ATHA, two separate streaks of luminosity are seen, labelled as the purple and green
 385 bands, but only the purple band follows the green grid.

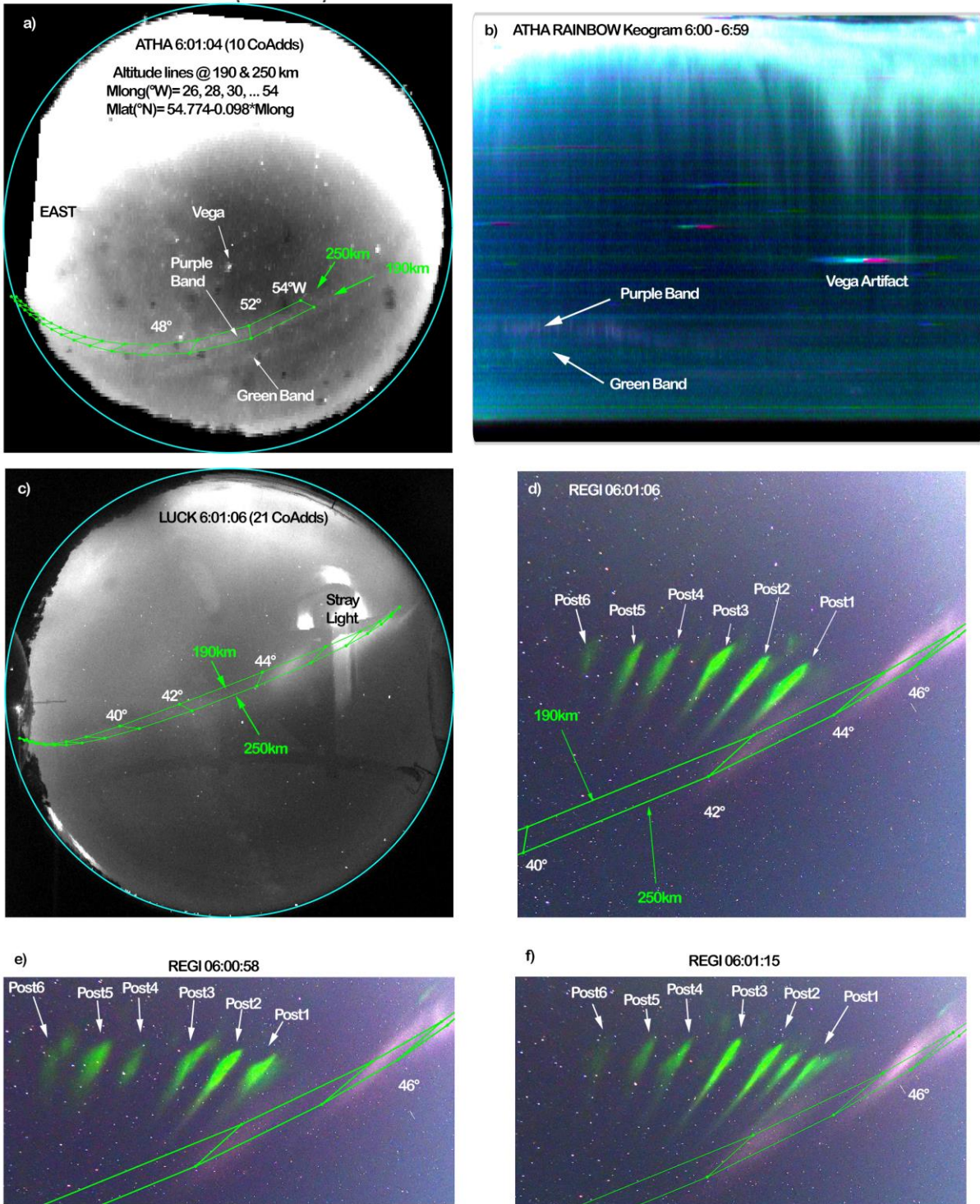
386
 387

388 The parameters for a linear fit of the magnetic latitude vs longitude for the prominent
 389 STEVE emission in this figure are shown in **figure 3a)** with the assumption that the altitude
 390 range is 190-250 km throughout the scene. Although slight “wiggles” about the purely linear fit

391 are apparent in the data, as most clearly seen in the LUCK 06:07:48 image in figure **3c**) or the
392 REGI image in figure **3d**), the departures are no more than 0.1° in terms of a latitude variation.
393 Alternatively, if not departures in latitude, the “wiggles” interpreted in terms of an altitudinal
394 variation would be no more than 50 km at the most extreme. Although the variation of magnetic
395 latitude vs. longitude at a typical auroral oval boundary could be curved rather than linear over a
396 40° span of longitude, a purely linear fit was all that was warranted here.

397 In addition to the synthetic ASI image comprised of a Maxima Merging of successive
398 registered REGI photographs near 6:07:48 shown in figure **3d**, several other MM composite
399 images could be formed. Every time successive photos were taken with significantly different
400 aim points of the camera useful MM composites can be formed.

401



402
 403 **Figure 4.** STEVE features are seen simultaneously in **a)** ATHA, **c)** LUCK and REGI. An ATHA
 404 keogram is shown in **b)**. Six green picket fence posts are indicated in **d)**, **e)** and **f)**. A grid of
 405 magnetic field line segments is shown in green. The specific green grid shown is chosen to pass
 406 through the purple band of luminosity seen in all three imagers and is the same fixed grid in all
 407 six panels of this figure.

408 2.6 Intermittency of green picket fence posts

409 Before the time of the images shown in figure 3, a number of green “picket fence post”
410 features began to appear in the REGI data as can be clearly seen in figure 4d. The original,
411 unregistered 6:01:06 REGI image used here is exactly the same as the central frame published in
412 figure 1 of (MacDonald E. N.-L., 2018, doi:10.1126/sciadv.aag0030) but labelled there with the
413 *incorrect* time 06:03:51 UTC. These green features are also seen in the ATHA data, but the
414 colored images are quite noisy, and it is preferable to use grayscale ATHA images (produced by
415 summation over the four color channels of the original ATHA data) to observe their spatial
416 structure. The full color (University of Calgary, 2020) ATHA keogram spanning the 6:00 to 6:59
417 time interval displayed in figure 4b confirms the difference in color seen far more clearly in the
418 REGI image between the upper and lower structures. The vertical scale of the keogram is
419 displayed so that it conforms to the vertical extent of the grayscale ATHA image to the left. As
420 Vega passes across the center of the ATHA imager it produces the rainbow-colored streak
421 artifact seen near 6:45 in the keogram. In the keogram spanning the 6:00 to 6:59 time interval, it
422 is seen that one band has a greenish tinge, while the other band has a purple hue. In the REGI
423 image at 6:01:06 shown, several distinct “green picket fence posts” are seen near the center of
424 the image. Occasionally, some of these posts are bright enough to be individually discernable in
425 the ATHA data, but with far less resolution. From successive REGI images, it is found that the
426 individual green picket fence posts vary significantly from frame to frame. The intermittency of
427 the picket fence posts is also apparent in the ATHA keogram.

428 The intermittency of the picket fence posts seen also accounts for the observation that
429 while there appears to be a nearly continuous band of green luminosity extending from horizon
430 to horizon seen in the coadded ATHA image shown in figure 3a) there is no discernable
431 evidence of green posts in the MM composite REGI synthetic ASI shown in figure 3d) despite
432 the far greater sensitivity to the green posts in the REGI data. The reason for this difference is
433 attributed to the fact that the 10 coadded ATHA frames represent an average over a 60 second
434 period, while the individual REGI frames each had an exposure of only four seconds. Just by
435 happenstance, none of the five individual REGI frames involved in the composite MM image
436 captured green picket fence posts, even though they are clearly visible in a REGI photo taken
437 just 22 seconds before the first frame of the panoramic sweep shown in figure 3d).

438 2.7 Exploitation of Magnetic Field Aligned Structures

439 The green picket fence post features appear very well aligned with the local magnetic
440 field lines. The quality of this alignment is best seen by the closeup regions of REGI data in
441 figures 5b), 6b), 6d) and 6f). Although it is conceivable that the green picket fence post features
442 are not actually field aligned structures but are instead all at a common altitude (say) but just by
443 happenstance spatially distributed so that they only “appear” to be aligned with the local
444 magnetic field, in view of the fact that numerous independent “posts” appear fleetingly from
445 frame to frame, and that so many of these posts are just as well aligned with local field lines as
446 the cases explicitly shown in figure 4d, it seems highly unlikely that these posts are NOT field
447 aligned. In a later section, a few cases in which the green posts are not so well aligned with local
448 magnetic field lines will be shown and discussed.

449 The presence of magnetic field aligned features allows another independent approach to
450 the determination of three-dimensional structure that is illustrated in figure 5. In this approach, it
451 is assumed that the green intensity seen in the REGI data can be attributed to the excitation of the
452 5577 Å spectral line by a population of precipitating electrons. High spectral resolution

453 measurements of green picket fence features by (Gillies, 2019, doi:10.1029/2019GL083272)
 454 show that the assumption of dominance for the 5577 Å emission is reasonable. That this
 455 emission is produced by precipitation rather than ionospheric skyglow is a topic of debate in the
 456 current literature, as summarized in the introduction. Here, we explore the ramifications of the
 457 assumption that this emission is in fact produced by electron precipitation.

458 The “global airglow” (GLOW) model (Solomon S. H., 1988,
 459 doi:10.1029/JA093iA09p09867), (Solomon S. , 2001, doi:10.1029/2000JA002011) is used to
 460 compute the volume emission rate as a function of altitude emerging from a population of
 461 precipitating electrons initially descending along a particular magnetic field line. We will
 462 consider both a Maxwellian energy distribution and a Monochromatic energy distribution for the
 463 incoming electrons at the top of the atmosphere. In order to relate the observed brightness along
 464 the length of a given green fence post to the brightness as a function of altitude, it is necessary to
 465 determine the relation between the position in the image of a given region of luminosity and the
 466 altitude of said luminosity.

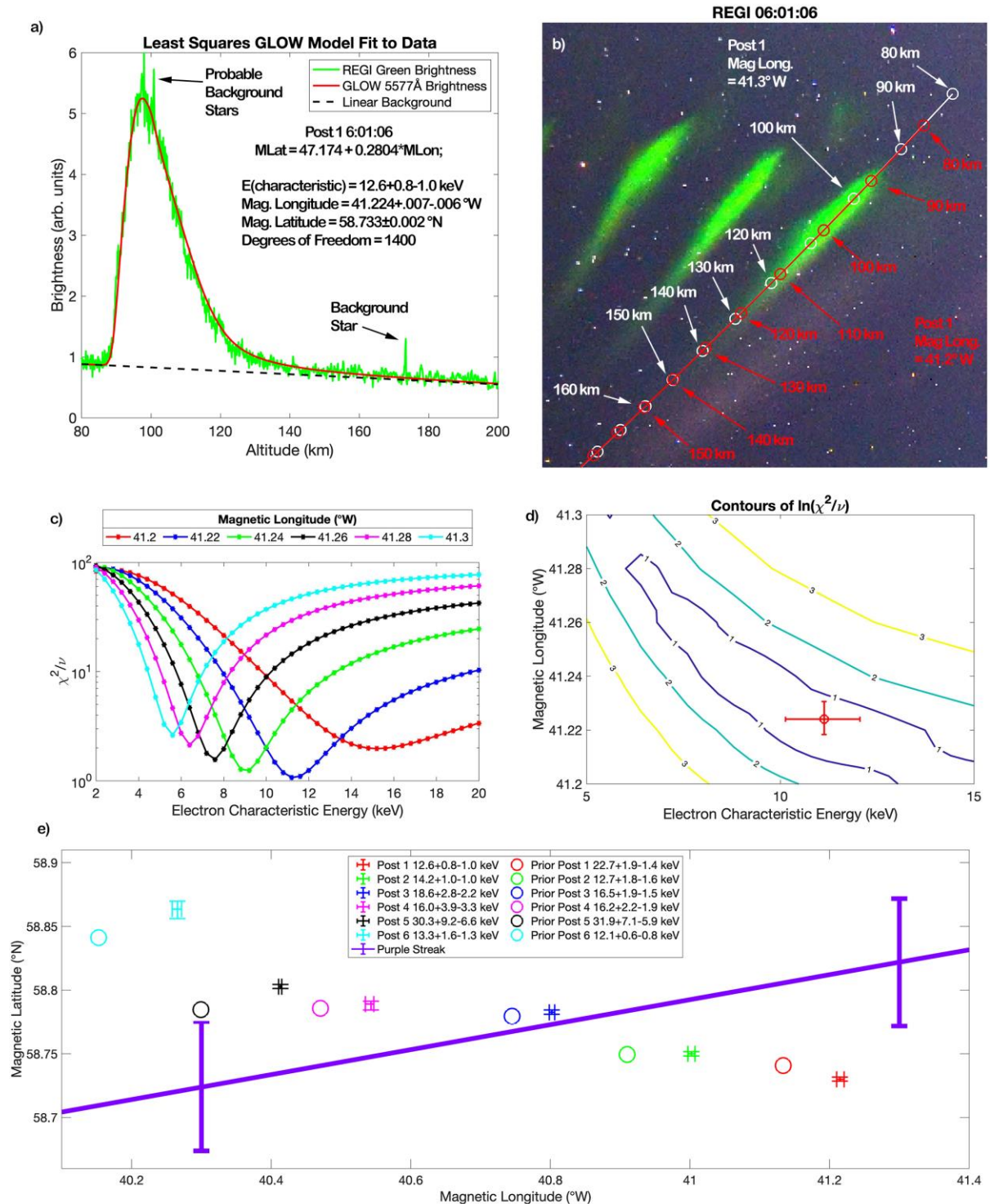
467 Requiring that a magnetic field line passes through a fixed point in a given photograph,
 468 such as a point near the center of a particular green fence post, constrains the relation between
 469 magnetic latitude and longitude. Over the range of coordinates considered here, this constraint
 470 produces a linear relation between the latitude and longitude. For the case shown in figure **5b**)
 471 this relation is

$$472 \quad \text{Magnetic Latitude } (^{\circ}\text{N}) = 47.174^{\circ} + 0.2804 * \text{Magnetic Longitude} (^{\circ}\text{W}). \quad (1)$$

473
 474 The linear coefficients vary strongly with the specific fixed-point choice. The values used for the
 475 other representative posts shown in figures **6b**), **6d**), and **6f**) are listed along with the resulting
 476 best fit parameters shown in figures **6a**), **6c**), and **6e**).

477 A specific choice of magnetic longitude then leads to a specific relation between the
 478 position along the field line and the altitude of that point. An illustrative example of these
 479 relations for the picket fence post labeled “post 1” in figure **4d**) is shown in figure **5b**). The field
 480 line having magnetic longitude 41.3°W passing through the center of post 1 is shown in white,
 481 with white circles for altitudes at intervals of 10 km from 80 km to 180 km indicated. The
 482 alternative field line having magnetic longitude 41.2°W also required to pass through the center
 483 of post 1 is shown in red, with red circles at altitudes 80 through 170 km shown.

484 The trajectories of these two field lines are virtually indistinguishable over the region
 485 shown in the figure. For the case shown, only at the top of the figure can the red and white
 486 magnetic field lines be seen to very slightly differ. Note that the altitude corresponding to a
 487 particular location is a very sensitive function of the choice of field line. For any given magnetic
 488 field line, the coordinates in the registered camera space are transformed by inverse gnomonic
 489 projection back to coordinates in the original photographic image using a piecewise linear
 490 interpolation between the locations of the vertices of the magnetic grid coordinates spaced by 10
 491 km in altitude, such as those shown in figure **5b**). The numerical value of the observed intensity
 492 at any given altitude is determined by “nearest neighbor” interpolation along the piecewise linear
 493 inverse gnomonic projection path through the original photographic data.
 494
 495



496
 497 **Figure 5.** The least squares fitting of Post 1 to a linear background plus GLOW model is
 498 illustrated here. In **b)** the location of two exemplary magnetic field lines passing through the
 499 middle of Post 1 are shown in red and white. The locations in the image of points at altitudes
 500 from 80 to 200 km at 10 km intervals along the two field lines are indicated to illustrate the
 501 sensitivity of the derived intensity vs. altitude function to the choice of magnetic field line. In **c)**

502 for each of six specific choices of magnetic longitude the χ^2/ν is plotted as a function of the
 503 GLOW model characteristic energy. In **d)** a contour plot of $\ln(\chi^2/\nu)$ is plotted as a function of
 504 energy and longitude. The red circled point represents the best fit value, with horizontal and
 505 vertical error bars representing the one-sigma uncertainty in energy and longitude respectively.
 506 The degree of covariance between these two variables can be seen by the slope in the “valley”. In
 507 **a)** the GLOW model calculation for the best fit case is shown, together with the fit parameters
 508 and uncertainties. In **e)** the best fit results for each of the six posts shown in figure **4d)** are plotted
 509 with horizontal and vertical error bars shown. Also plotted as circles are the best fit results for
 510 each of the six “prior” posts shown in figure **4e)** corresponding to the photograph taken 8.34
 511 seconds earlier. Finally, the location of the magnetic grid that best aligns with the swath of the
 512 purple streak of luminosity across ATHA, LUCK and REGI seen in figure **4** is shown in **5e)** by
 513 the purple line and error bars in the region of the six posts.

514

515 For six magnetic longitude choices evenly spaced between the extremes shown in figure
 516 **5b)**, a series of least squares fits of GLOW model calculations to the observed luminosity were
 517 made with characteristic electron energies ranging from 0.4 to 20 keV in steps of 0.4 keV. The
 518 intensity along a given field line was extracted and converted to the intensity as a function of
 519 altitude. Inconveniently located bright stars can sometimes not be avoided, and the observed
 520 intensity near such stars (typically only a few pixels out of approximately 1400 pixels, depending
 521 on the choice of field line) is replaced with a value linearly interpolated from the surrounding
 522 neighborhood. The number of degrees of freedom for the fit is reduced by the number of such
 523 “patched” pixels. For a given magnetic field line and characteristic electron energy, the three
 524 fitting parameters were: a slope and offset for the assumed linear background and an electron
 525 flux level for the strength of the GLOW model calculation.

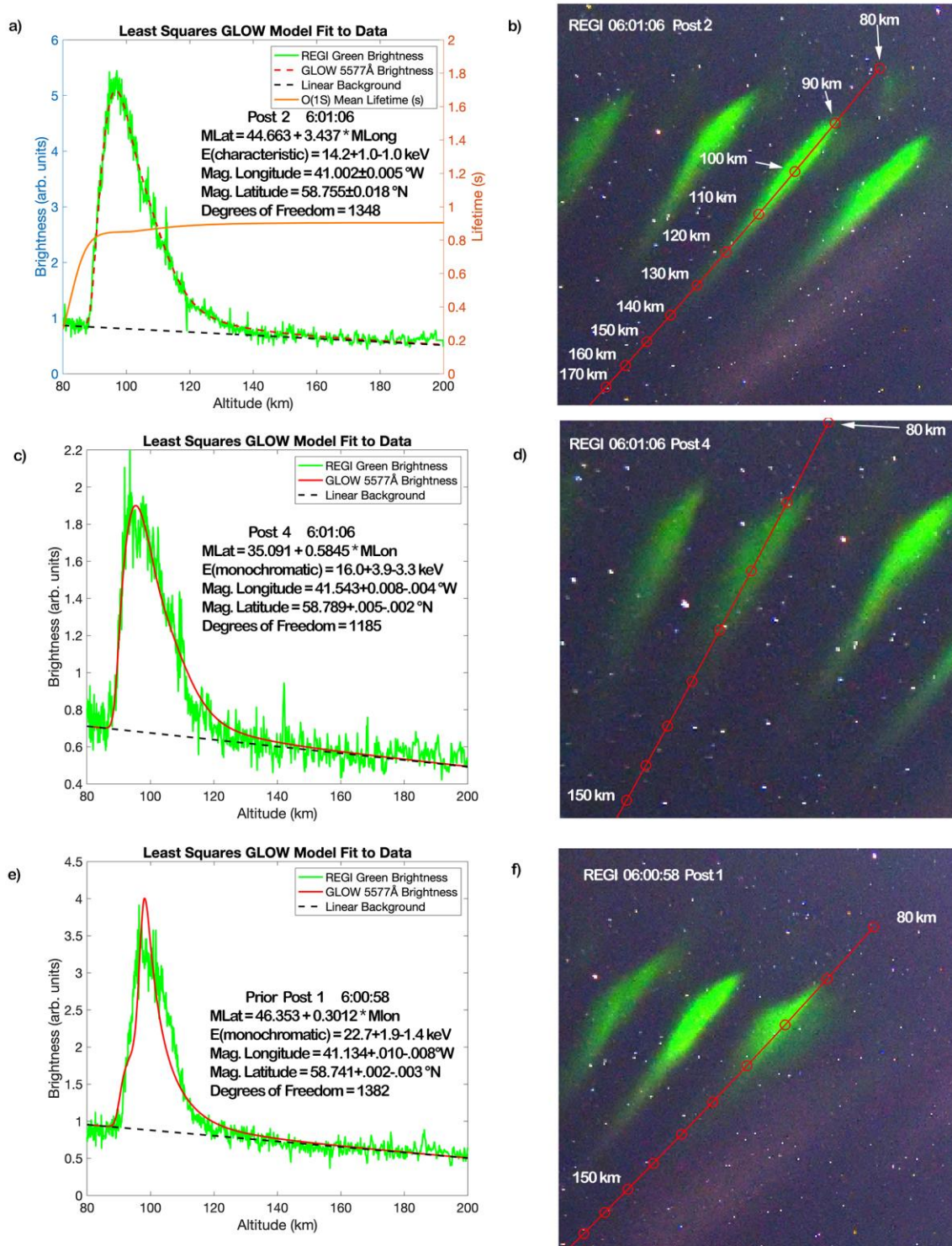
526 The sum of squared residuals normalized per degree of freedom χ^2/ν is plotted for each
 527 of these fits in figure **5c)**. A contour plot of χ^2/ν is plotted in figure **5d)** as a function of the
 528 electron characteristic energy and magnetic longitude. A noise level common to all fits displayed
 529 in **5c)** and **5d)** was chosen to make the overall minimum χ^2/ν be unity. This noise level includes
 530 not only the camera readout noise and photon shot noise, but also the “clutter” noise from the
 531 host of underlying stars and other celestial objects that might underlie the region of green post
 532 luminosity. The minimum χ^2/ν determines the best fit values for the electron energy and the
 533 magnetic longitude. The best fit GLOW model, assuming a Maxwellian energy flux distribution,
 534 is compared with the observed brightness as a function of altitude corresponding to the best fit
 535 magnetic field line coordinates in **5a)**. In this plot, no correction for the “background” star
 536 appearing just above the 170 km altitude level, nor for the pair of likely stars located near the
 537 peak intensity. Although bright star contamination can easily be detected and “patched” over,
 538 dimmer background stars are not so easily removed. For this reason, the “clutter noise” of
 539 unresolved background stars is usually larger than the noise from background dark current
 540 fluctuations. All this said, the residuals between the GLOW model fit plus linear background and
 541 the observed REGI green brightness are approximately normally distributed, with the occasional
 542 isolated bright star outliers, so that the “one sigma” uncertainties in both characteristic energy
 543 and magnetic longitude may be estimated from the point at which χ^2 increases by $\sqrt{2\nu}$ above its
 544 minimum value. These uncertainties are not necessarily symmetric about the best fit value. These
 545 best fit values and uncertainties are numerically shown in **5a)** and indicated with the red circle
 546 with horizontal and vertical error bars in **5d)**.

547 Note that this method for determination of the altitude distribution of STEVE intensity
548 using magnetic field aligned structures in the REGI data is completely independent of the
549 triangulation approach described above. In contrast to the triangulation approach it can be
550 performed using data from a single high-quality digital photograph without the requirement of
551 data from another site. It is only required that the model used, e.g. GLOW, produces a reasonable
552 estimate for the variation of brightness as a function of altitude. The altitude distribution found in
553 this way is in good agreement with the altitude range found using triangulation between
554 simultaneous images taken from separate locations, such as the example shown in figure 4.

555 A similar analysis for posts 2 through 6 of figure 4d) seen at 6:01:06 leads to the points
556 plotted with horizontal and vertical error bars in figure 5e). Also shown in this figure are prior
557 versions of posts 1 through 6 in figure 4e) seen at 6:00:58 but plotted as circles having the same
558 color as the error bar plots for the presumably later versions of the same posts. For some posts,
559 the Maxwellian energy distribution assumption produces a brightness distribution that is too
560 broad in altitude to provide an acceptable fit to the observed brightness distribution. Such a case
561 is post 4 at 6:01:06 shown in figure 6c). Instead, a GLOW model assuming a Monochromatic
562 energy distribution incident at the top of the atmosphere produces a narrower peak, and the fit to
563 the observed brightness is much better. In other cases, neither the Maxwellian nor
564 Monochromatic distributions provide acceptable fits, as can be seen for the prior version of post
565 1 seen at 6:00:58 shown in figure 6e). In this case, the observed REGI brightness appears to be
566 broader than a purely Monochromatic distribution, but narrower than a purely Maxwellian
567 distribution.

568 Qualitatively, the posts seen in figure 4d, 4e or 4f that are best fit with Maxwellian
569 distributions appear as more extended streaks with long tails, while those that are best fit with
570 Monochromatic distributions appear as less extended streaks, such as “prior” posts 1, 4 and 6
571 seen at 6:00:58. Whether a Maxwellian or Monochromatic energy flux distribution is used in
572 fitting, the deduced magnetic field line coordinates are not significantly affected. In any case, the
573 quite well-defined magnetic coordinates of the green posts strongly overlap with the less
574 precisely determined magnetic coordinates of the swath of purple STEVE luminosity. The green
575 posts appear to share magnetic field lines with the purple streaks, even though not at the same
576 time.

577
578 Although there are certain regions where the purple band of luminosity appears to be
579 approximately aligned with local magnetic field lines, there are other regions where the purple
580 band is clearly not so well aligned. In figure 4d) for example, just west of the 44° line of
581 longitude, a patch of purple seems to extend approximately parallel to the local magnetic field
582 lines. However, just to the west of the 46° line of longitude there is a streak of purple brightness
583 that seems to be nearly at right angles to the local magnetic field lines. This pattern of alignments
584 is also apparent in figures 4e) and 4f). Without confidence that the purple streaks of STEVE are
585 field aligned, an attempt to perform an analysis using the GLOW model similar to that done for
586 the green fence posts is problematic.



587
 588 **Figure 6.** Details for three posts are shown. In **a)** for post 2 at 6:01:06 the best fit case is
 589 displayed for a Maxwellian distribution. The locations of the best fit magnetic field line
 590 coordinates at altitudes from 80 to 200 km are displayed by the red line and circles superimposed
 591 on the observed data in **b)**. Similar fits using Monochromatic electron energy distributions are
 592 shown for Post 4 at 6:01:06 in **c)** and **d)** and for Post 1 at 6:00:58 in **e)** and **f)**.

593 2.8 Temporal Analysis of Photographs

594 Assuming the validity of the GLOW model approach, some of the variations in the shape
595 of specific green picket fence posts observed in the individual images can be interpreted in terms
596 of underlying temporal variations. The GLOW model prediction for the mean lifetime of the
597 O(1S) state responsible for the 5577 Å emission is plotted as a function of altitude as the orange
598 curve in figure 6a). For all altitudes of interest, the O(1S) state lifetime is less than the 4 second
599 exposure time and 8.34 second cadence of the REGI images shown in these figures. For this
600 reason, the 5577 Å oxygen atomic emission seen in successive images are coming from O(1S)
601 excitations occurring during (or slightly earlier than) the exposure durations of each separate
602 image. In effect, each frame containing 5577 Å emission serves as a “streak camera” image that
603 can provide detailed temporal information at a much finer time scale than the exposure time of
604 the individual images. As an example, the “blurring” seen to the right of the brighter end of Post
605 1 in figure 4f) can be interpreted as “motion blurring” as the precipitating electrons responsible
606 for the green emission follow a series of magnetic field lines at successively further westward
607 longitudes. Similarly, the blurring seen to the left of the bright end of Post 4 in figure 4f) can be
608 interpreted as emission happening somewhat earlier than the stronger emission along the
609 brightest portions of Post 4.

610 The speed of the apparent longitudinal motion of the precipitating electrons responsible
611 for posts 1 through 6 can be quantified by the separation in figure 5e) between the prior versions
612 and later versions of each post. The average longitudinal motion for the six posts corresponds to
613 a longitudinal angular speed of 0.0115 °/s, or a translational speed of 0.67 km/s at the altitude of
614 the posts. This translational speed is an order of magnitude less than the ion drift speed measured
615 by the SWARM-A satellite as it crossed over a region of STEVE emission at 6:43:22 as reported
616 in (MacDonald E. N.-L., 2018, doi:10.1126/sciadv.aag0030).

617 3 Summary

618 We have found that a wealth of data can be extracted from digital images recorded by
619 photographers who have fortuitously been able to photograph night sky events of a rare and
620 transient nature, as typified by the skyglow phenomenon known as STEVE. Stars and planets
621 seen in the images may be used to register pixels to angular coordinates of altitude and azimuth
622 to within an arcminute. Satellites that appear in the images may be used to synchronize, or check
623 the synchronization of, photographs to within one second.

624 Application of these methods to the analysis of the 25 July 2016 STEVE event leads to a
625 confirmation of the “double layer” altitude structure of the purple and green streaks previously
626 reported in the literature. From the high spatial resolution photographs, we are able to quantify
627 the energy of the electrons responsible for the green streaks to high precision. We are also able to
628 quantify the apparent speed of the green streaks. Finally, we have found that the green streaks
629 appear and disappear in a correlated fashion over a very broad horizon to horizon swath of
630 longitudes.

631 As advice to citizen science auroral photographers on how to provide the most useful
632 series of images for scientific analysis, it is quite helpful to have the following:

- 633 1. A time lapse sequence using a tripod, with fixed camera settings
- 634 2. A panorama across the sky with fixed exposure settings
- 635 3. At least one photograph containing the International Space Station for accurate time
636 synchronization, or alternatively a well-defined time stamp

- 637 4. Accurate knowledge of the geodetic coordinates from which the images are taken,
638 or if the camera has built-in GPS, a well-defined location stamp
639 5. Finally, if an unusual event of any sort is captured, please find a relevant scientific
640 organization that can archive your data for distribution and for posterity

641 With this information, there is no doubt that high resolution, high sensitivity ground-based
642 photographs of STEVE will continue to provide valuable scientific contributions to our
643 understanding of these fascinating events.

644 **Acknowledgments, Samples, and Data**

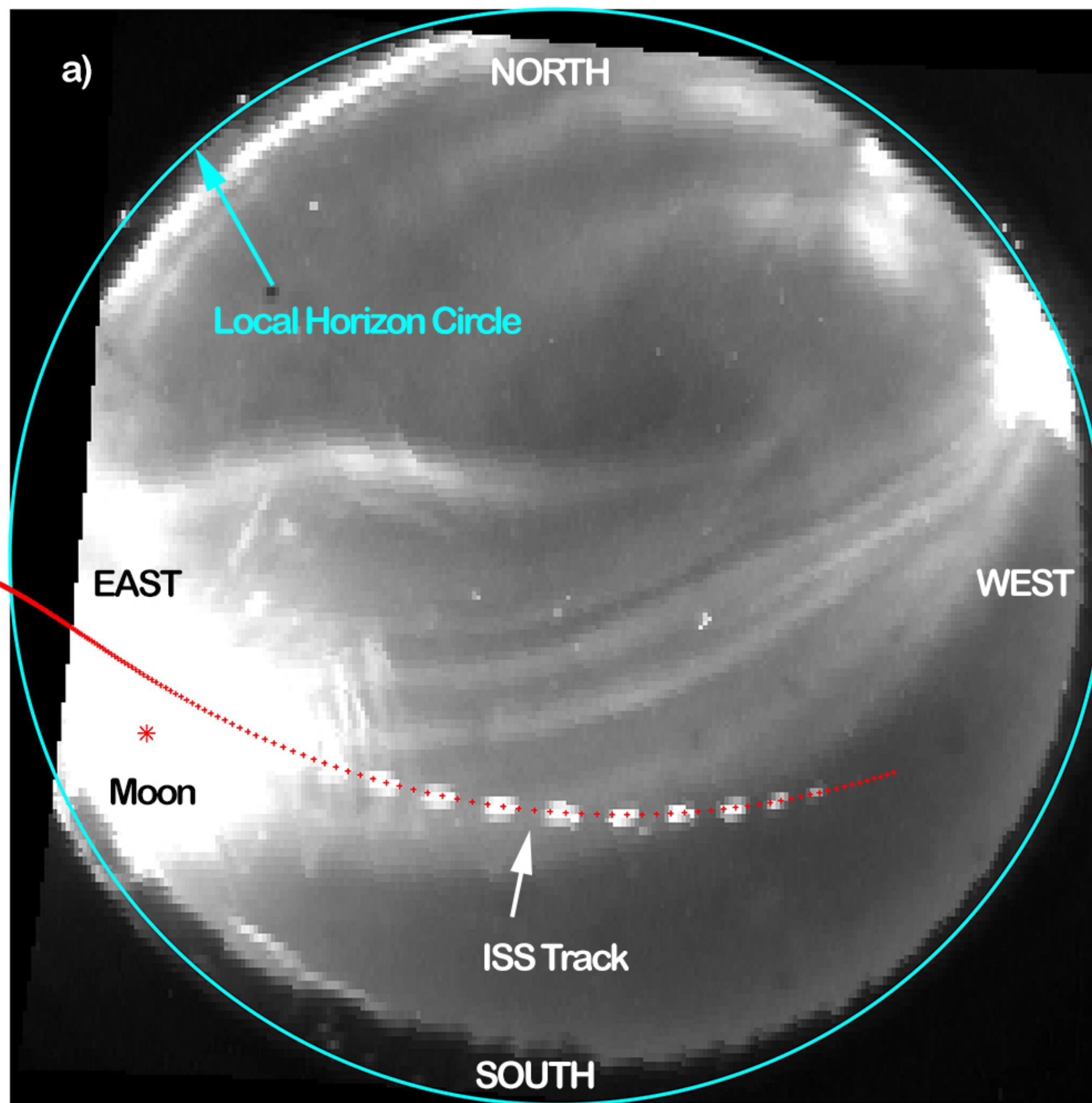
- 645 • The authors declare no competing interests.
- 646 • The image processing functions used to register the photographs discussed in this work
647 are included in the supplemental information.
- 648 • The 16-bit registered REGI photographs used in this work are available from
649 <https://doi.org/10.6084/m9.figshare.11674206> (Bennett, Registered Photographs from
650 "Improved Analysis of STEVE Photographs" JGR Article, 2020)

651 **References**

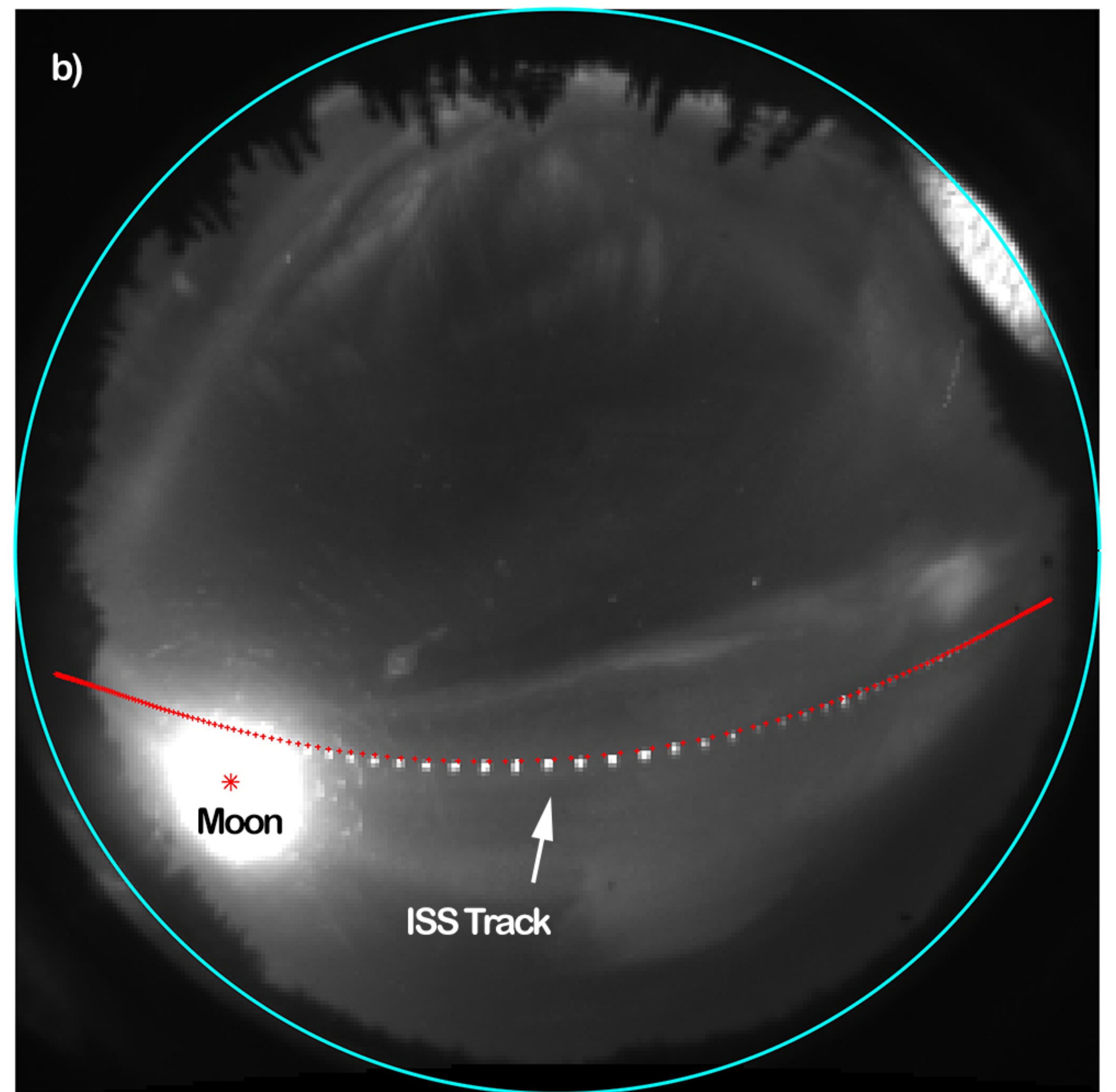
- 652 Aida, S. &. (2013). Accuracy Assessment of SGP4 Orbit Information Conversion into Osculating Elements. *6th*
653 *European Conference on Space Debris*. Darmstadt, Germany: ESA.
- 654 Archer, W. S.-L. (2019, doi:10.1029/2019GL084473). The Vertical Distribution of the Optical Emissions of a Steve
655 and Picket Fence Event. *Geophysical Research Letters*, 10,719-10,725.
- 656 Bennett, C. (2020). Low Energy Electron Precipitative Excitation of Purple STEVE Bands. *Journal of Geophysical*
657 *Research*.
- 658 Bennett, C. (2020, January). *Registered Photographs from "Improved Analysis of STEVE Photographs" JGR Article*.
659 Retrieved from figshare:
660 [https://figshare.com/articles/Registered_Photoshops_from_Improved_Analysis_of_STEVE_Photoshops_](https://figshare.com/articles/Registered_Photoshops_from_Improved_Analysis_of_STEVE_Photoshops_JGR_Article/11674206)
661 [JGR_Article/11674206](https://figshare.com/articles/Registered_Photoshops_from_Improved_Analysis_of_STEVE_Photoshops_JGR_Article/11674206)
- 662 Bettonvil, F. (2005). Imaging Fisheye Lenses. *WGN, Journal of the International Meteor Organization*, 33(1), 9-
663 14.
- 664 Chu, X. D.-L. (2019, doi:10.1029/2019GL082789). Identifying the magnetospheric driver of STEVE. *Geophysical*
665 *Research Letters*.
- 666 Crouse, D. (2017, May). The Tracker Component Library: Free Routines for Rapid Prototyping. *IEEE Aerospace*
667 *and Electronic Systems Magazine*, 32(5), 18-27.
- 668 Gallardo-Lacourt, B. L. (2018, doi:10.1029/2018GL078509). On the Origin of STEVE: Particle Precipitation or
669 Ionospheric Skyglow? *Geophysical Research Letters*, 1-6.
- 670 Gillies, D. D.-L. (2019, doi:10.1029/2019GL083272). First Observations From the TReX Spectrograph: The Optical
671 Spectrum of STEVE and the Picket Fence Phenomena. *Geophysical Research Letters*, 7207-7213.
- 672 Hankey, M. (2019, November 6). *METEOR FAQS*. Retrieved from [https://www.amsmeteors.org/meteor-](https://www.amsmeteors.org/meteor-showers/meteor-faq/#3)
673 [showers/meteor-faq/#3](https://www.amsmeteors.org/meteor-showers/meteor-faq/#3)
- 674 Hoffleit, D. &. (2014, January). *Yale Bright Star Catalog*. Retrieved from [http://tdc-](http://tdc-www.harvard.edu/catalogs/bsc5.html)
675 [www.harvard.edu/catalogs/bsc5.html](http://tdc-www.harvard.edu/catalogs/bsc5.html)
- 676 Kelso, T. (2019, 8). *CelesTrak Home Page*. Retrieved from Celestrak: <https://celestrak.com>
- 677 Lodriguss, J. (2020, 1 14). *Nikon D810a Review*. Retrieved from Catching the Light:
678 http://www.astropix.com/html/i_astrop/eq_tests/Nikon_D810a_Review.html
- 679 MacDonald, E. C. (2015, doi:10.1002/2015SW001214, September 7). Aurorasaurus: A citizen science platform for
680 viewing and reporting the aurora. *Space Weather*, 13, 548-559.
- 681 MacDonald, E. N.-L. (2018, doi:10.1126/sciadv.aag0030). New science in plain sight: Citizen scientists lead to the
682 discovery of optical structure in the upper atmosphere. *Science Advances*, 1-5.
- 683 Mathworks. (2019, July). *Mathworks*. Retrieved from mathworks.com
- 684 Maus, S. (2010, doi: 10.1029/2010GC003026). An ellipsoidal harmonic representation of Earth's lithospheric
685 magnetic field to degree and order 720. *Geochemistry, Geophysics, Geosystems*.
- 686 Mende, S. H. (2019, doi:10.1029/2019GLO86145). Subauroral Green STEVE Arcs: Evidence for Low-Energy
687 Excitation. *Geophysical Research Letters*.
- 688 Nikon. (2019, 12 14). *Download Center*. Retrieved from nikonusa.com:
689 https://downloadcenter.nikonimglib.com/en/products/162/Capture_NX-D.html
- 690 Nishimura, Y. G.-L. (2019, doi:10.1029/2019GL082460). Magnetospheric Signatures of STEVE: Implications for
691 the Magnetospheric Energy Source and Interhemispheric Conjugany. *Geophysical Research Letters*, 5637-
692 5644.
- 693 Solomon, S. (2001, doi:10.1029/2000JA002011). Auroral particle transport using Monte Carlo and hybrid methods.
694 *Journa of Geophysical Research*, 106, 107-116.
- 695 Solomon, S. H. (1988, doi:10.1029/JA093iA09p09867). The auroral 6300 A emission- Observations and modeling.
696 *J. Geophys. Res.*, 9867-9882.
- 697 University of Calgary. (2018, 12 9). *UofC Space Physics Data Portal*. Retrieved from [https://data-](https://data-portal.phys.ucalgary.ca)
698 [portal.phys.ucalgary.ca](https://data-portal.phys.ucalgary.ca)
- 699 University of Calgary. (2020, May 1). *UofC Space Physics Group Data Landing Page Ground-Based Observations*.
700 Retrieved from UofC Space Physics Group Data Landing Page:
701 [http://data.phys.ucalgary.ca/sort_by_instrument/all_sky_camera/GO-](http://data.phys.ucalgary.ca/sort_by_instrument/all_sky_camera/GO-Canada_AGO/stream2.colour_corrected/2016/07/25/atha_rainbow-01/ut06/20160725_06_atha_rainbow-01_full-keogram.pnm.jpg)
702 [Canada_AGO/stream2.colour_corrected/2016/07/25/atha_rainbow-01/ut06/20160725_06_atha_rainbow-](http://data.phys.ucalgary.ca/sort_by_instrument/all_sky_camera/GO-Canada_AGO/stream2.colour_corrected/2016/07/25/atha_rainbow-01/ut06/20160725_06_atha_rainbow-01_full-keogram.pnm.jpg)
703 [01_full-keogram.pnm.jpg](http://data.phys.ucalgary.ca/sort_by_instrument/all_sky_camera/GO-Canada_AGO/stream2.colour_corrected/2016/07/25/atha_rainbow-01/ut06/20160725_06_atha_rainbow-01_full-keogram.pnm.jpg)
- 704 Weisstein, E. (2019, July 22). *Gnomonic Projection*. Retrieved from
705 <http://mathworld.wolfram.com/GnomonicProjection.html>

Figure 1.

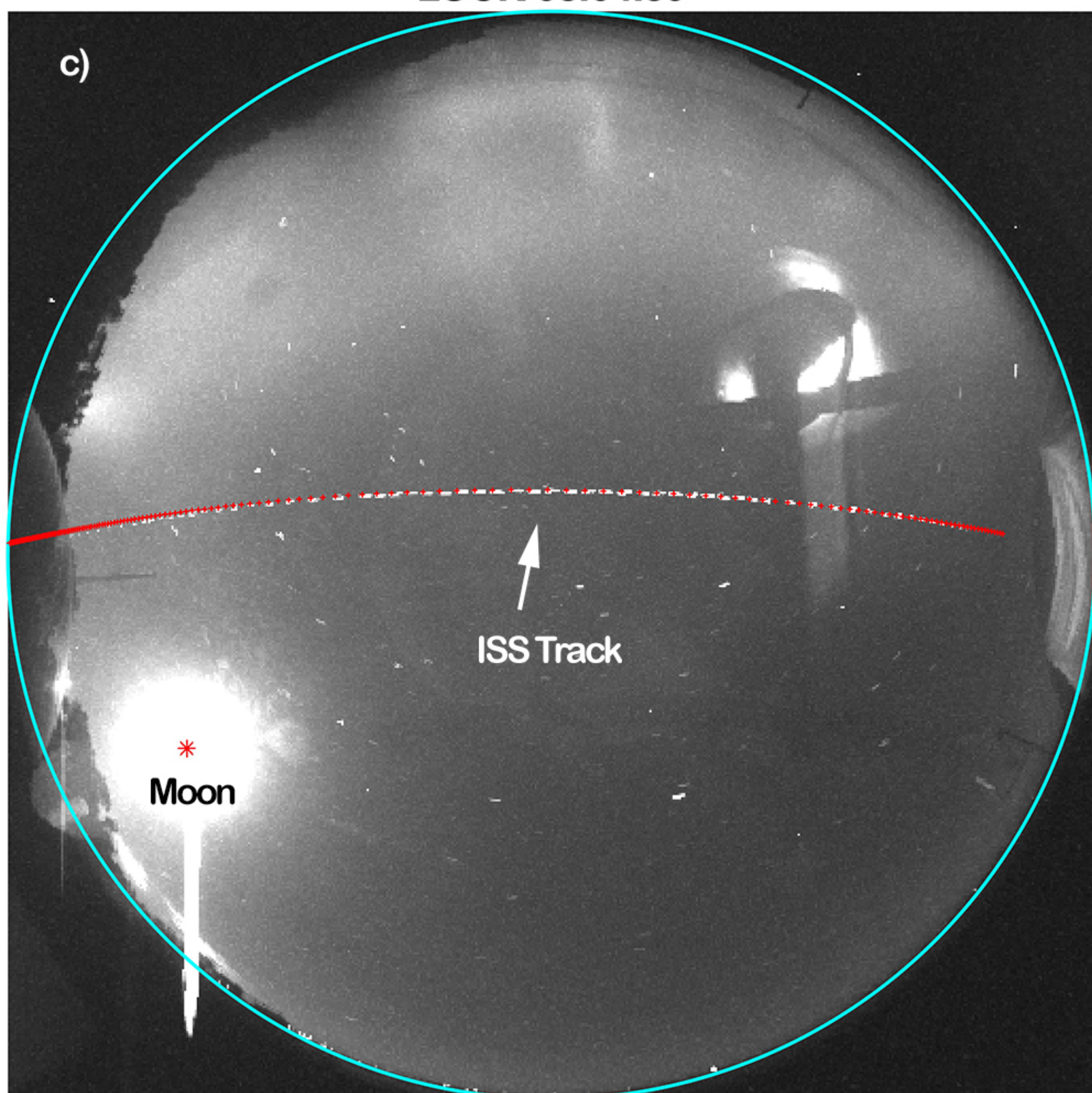
ATHA 08:03:34



TPAS 08:05:41



LUCK 08:04:39



PINA 08:06:15

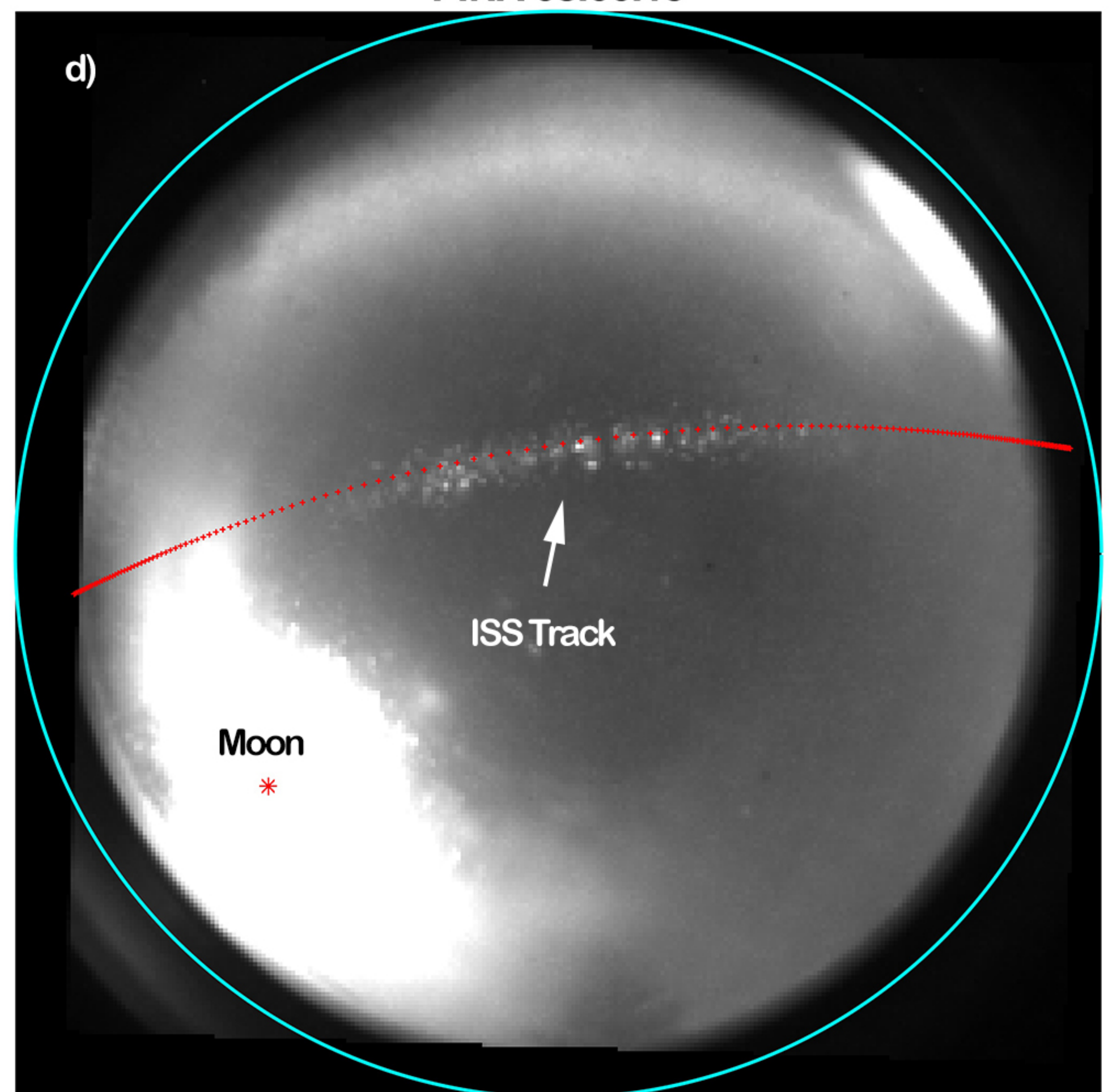
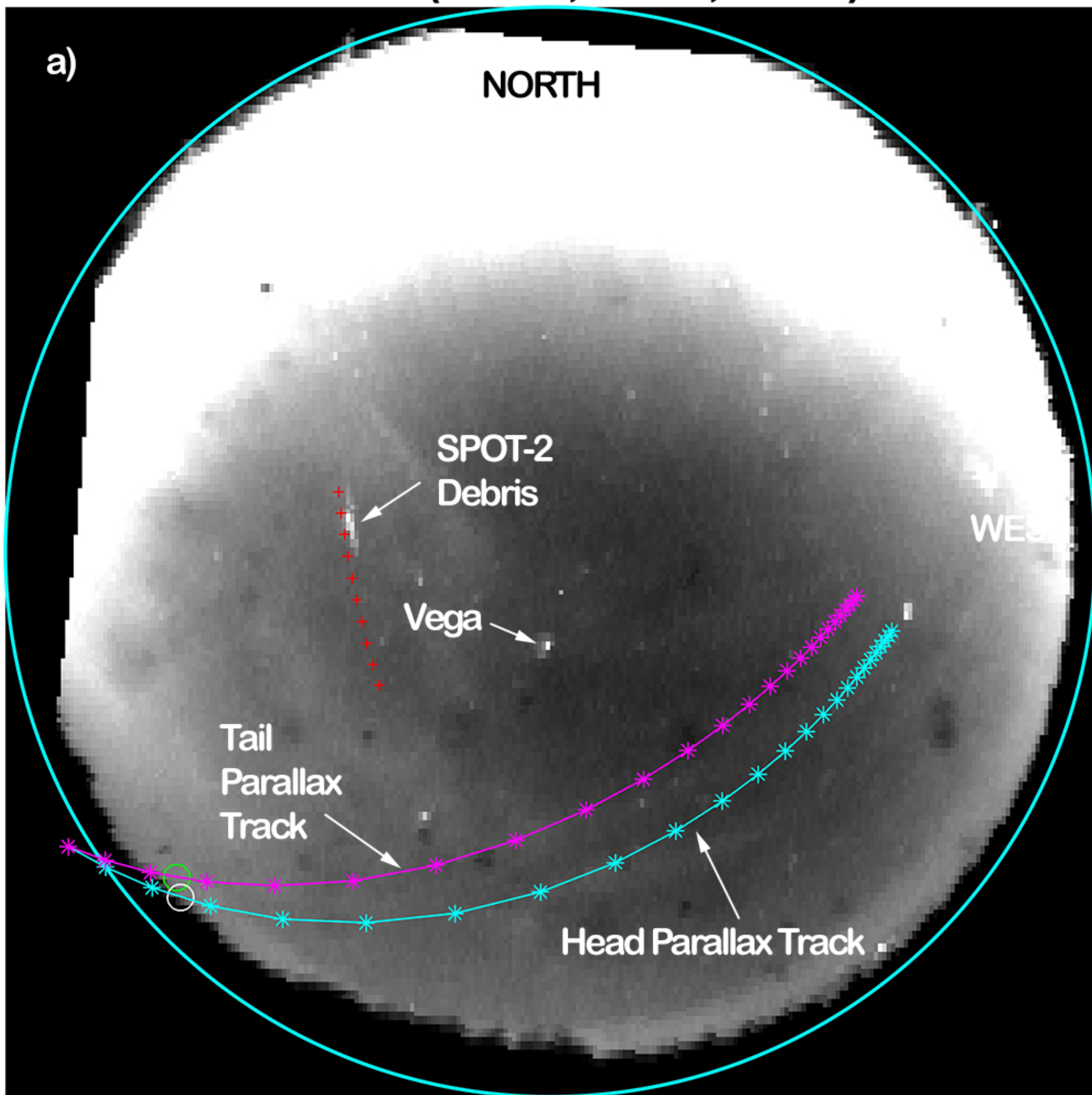
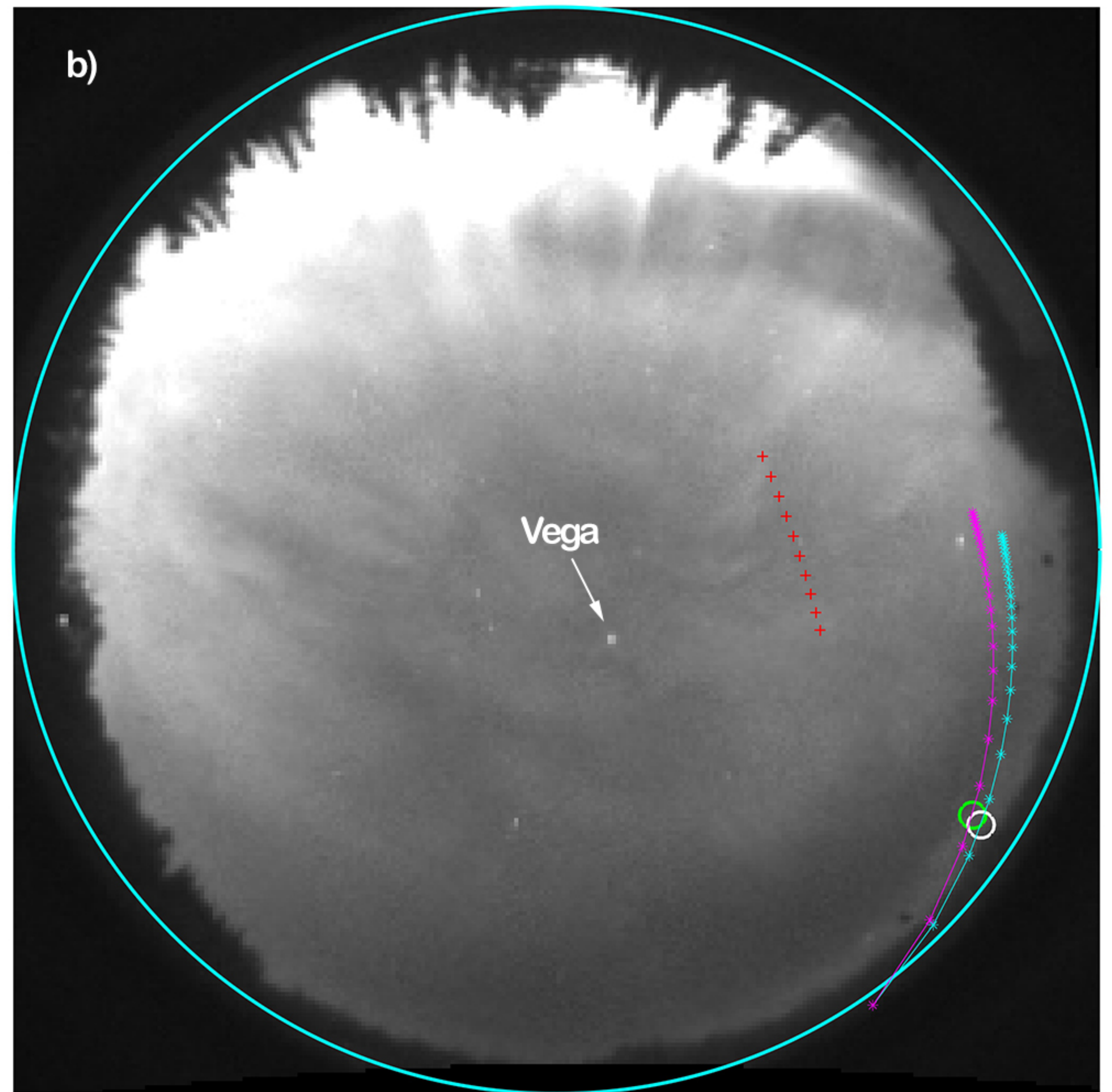


Figure 2.

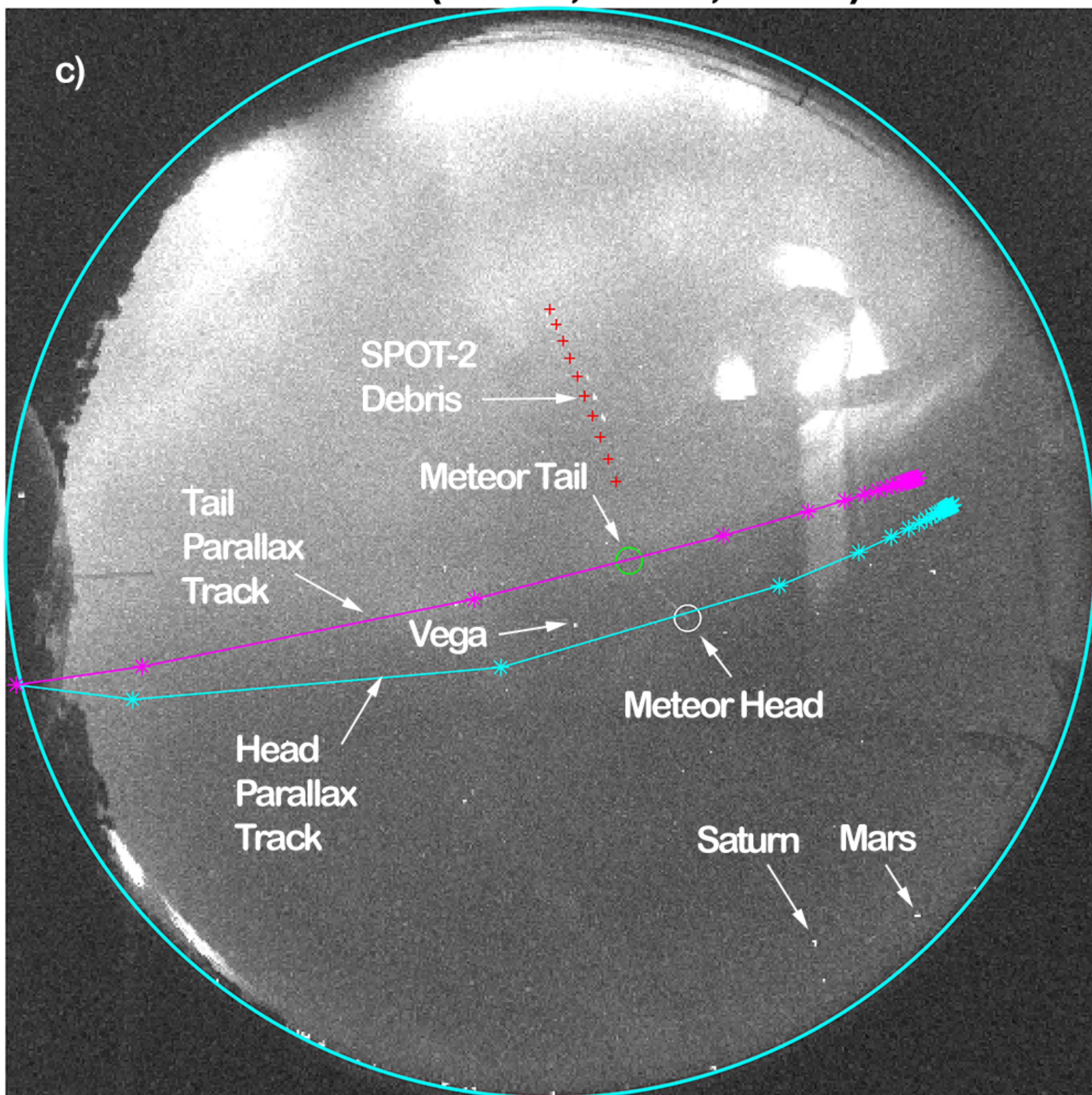
ATHA MM(5:54:16,5:54:22,5:54:28)



TPAS 05:54:38



LUCK MM(5:54:36,5:54:42,5:54:48)



REGI MM(5:54:37,5:54:46,5:54:54,5:55:02)

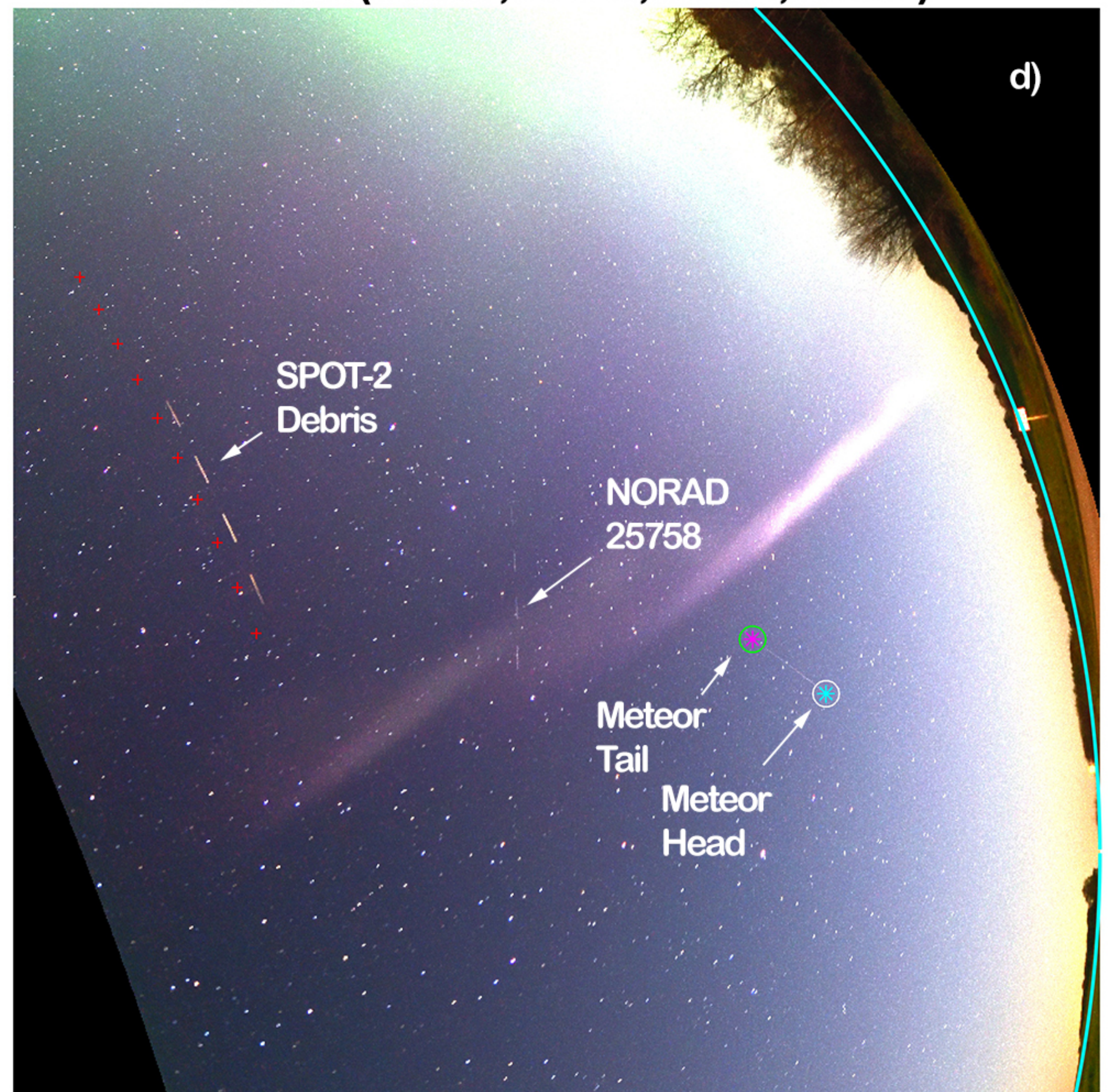
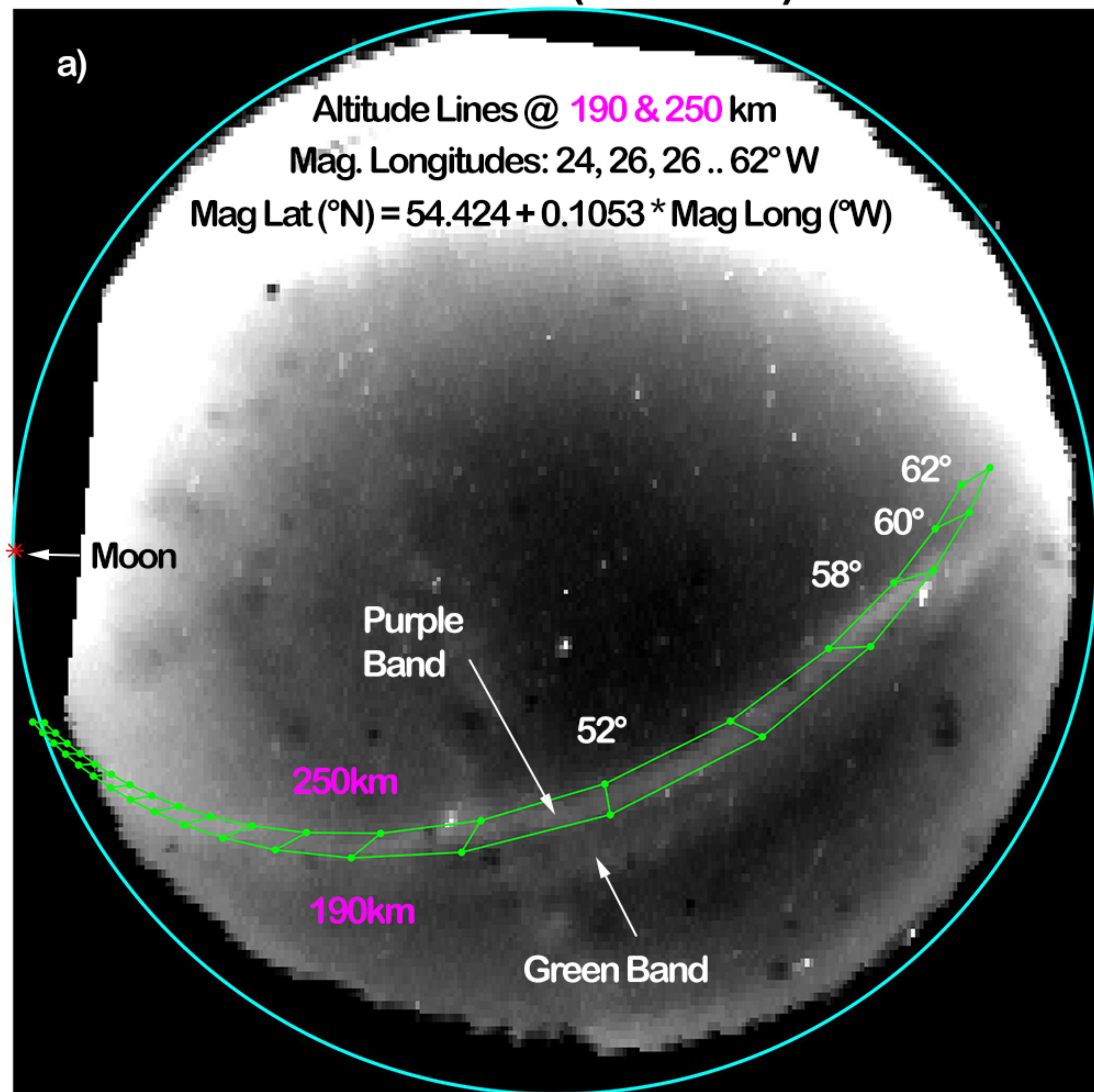
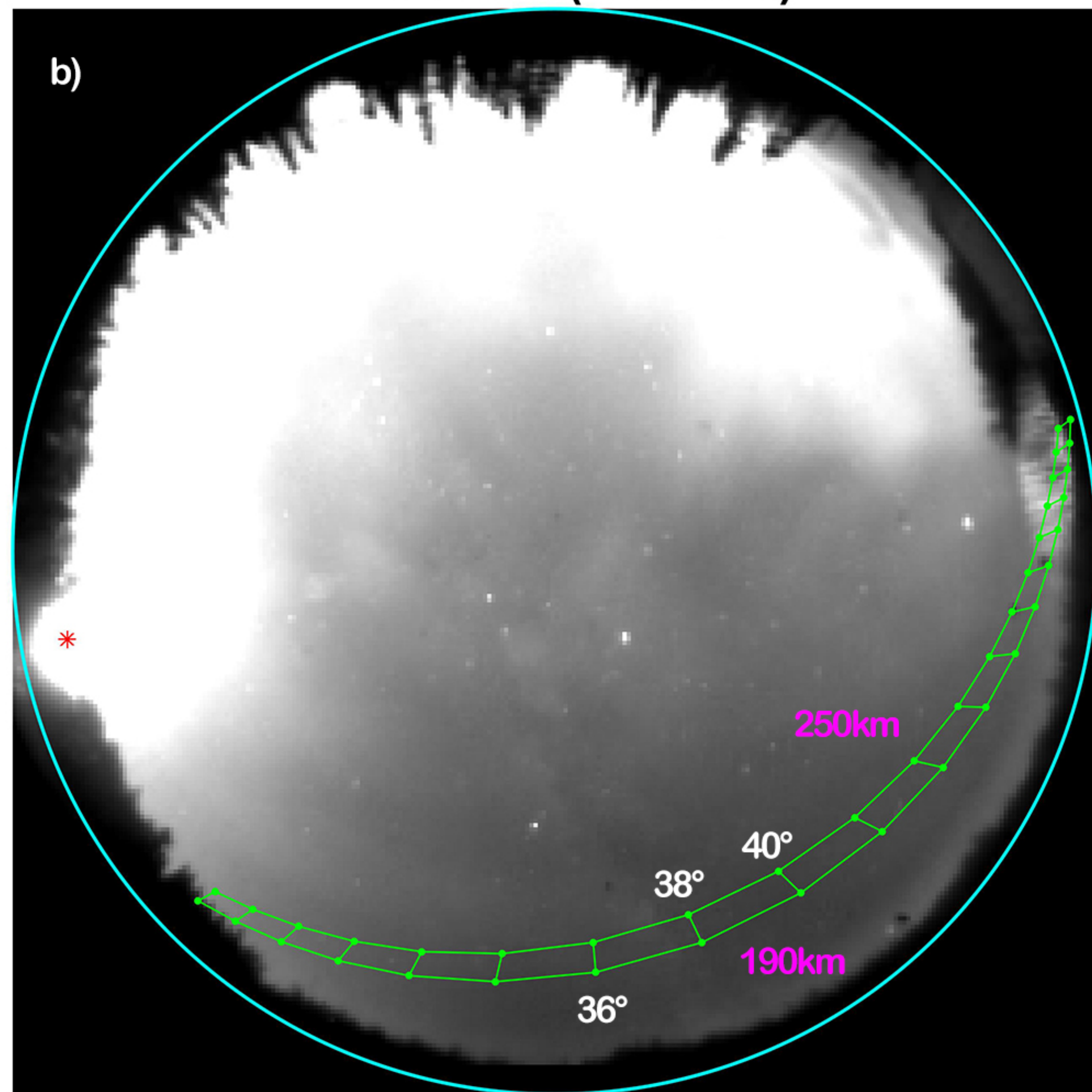


Figure 3.

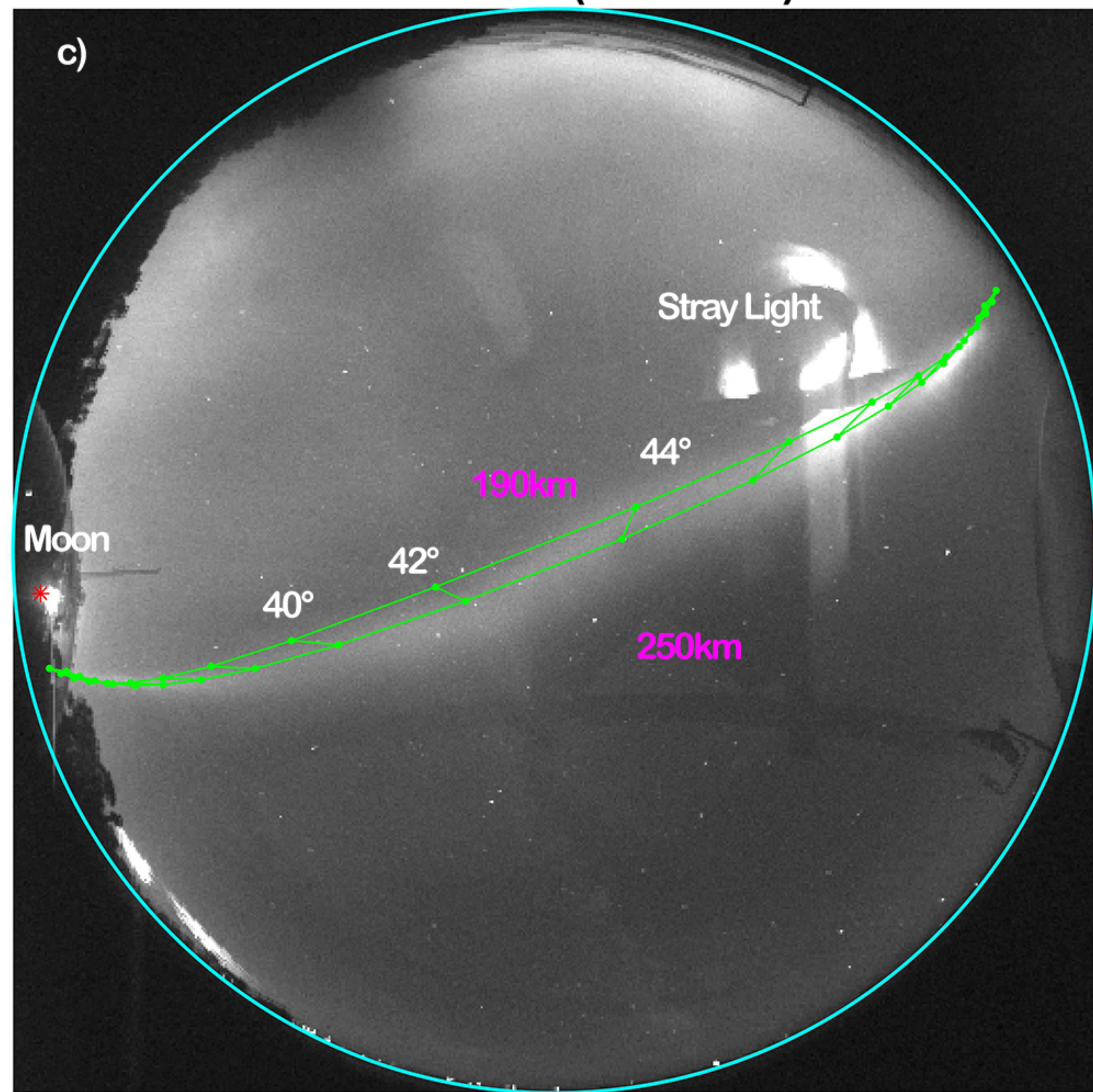
ATHA 6:07:48 (10 CoAdds)



TPAS 6:07:48 (21 CoAdds)



LUCK 6:07:48 (21 CoAdds)



REGI MM(6:07:18,6:07:26,6:07:32,6:07:46,6:07:53)

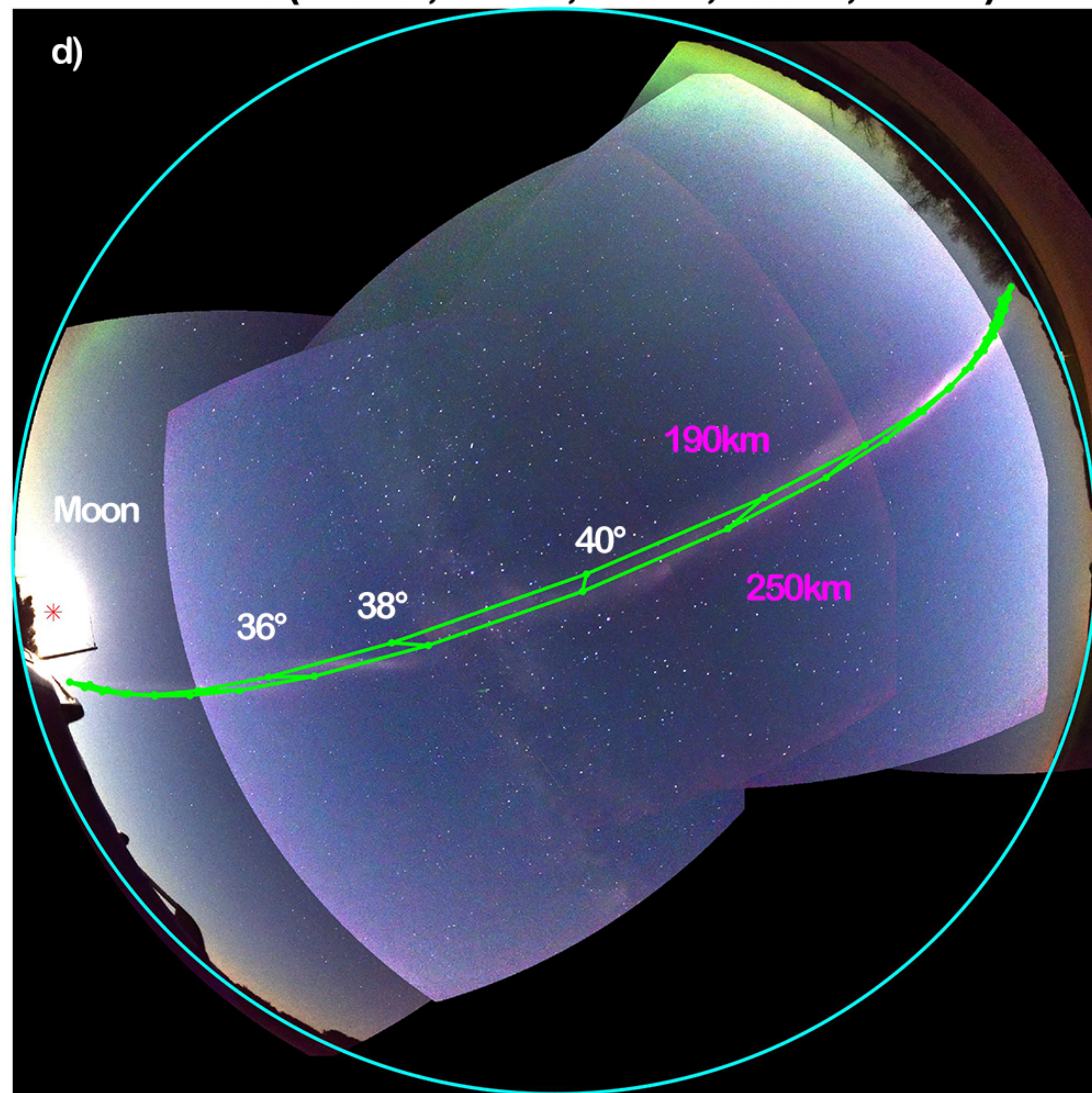


Figure 4.

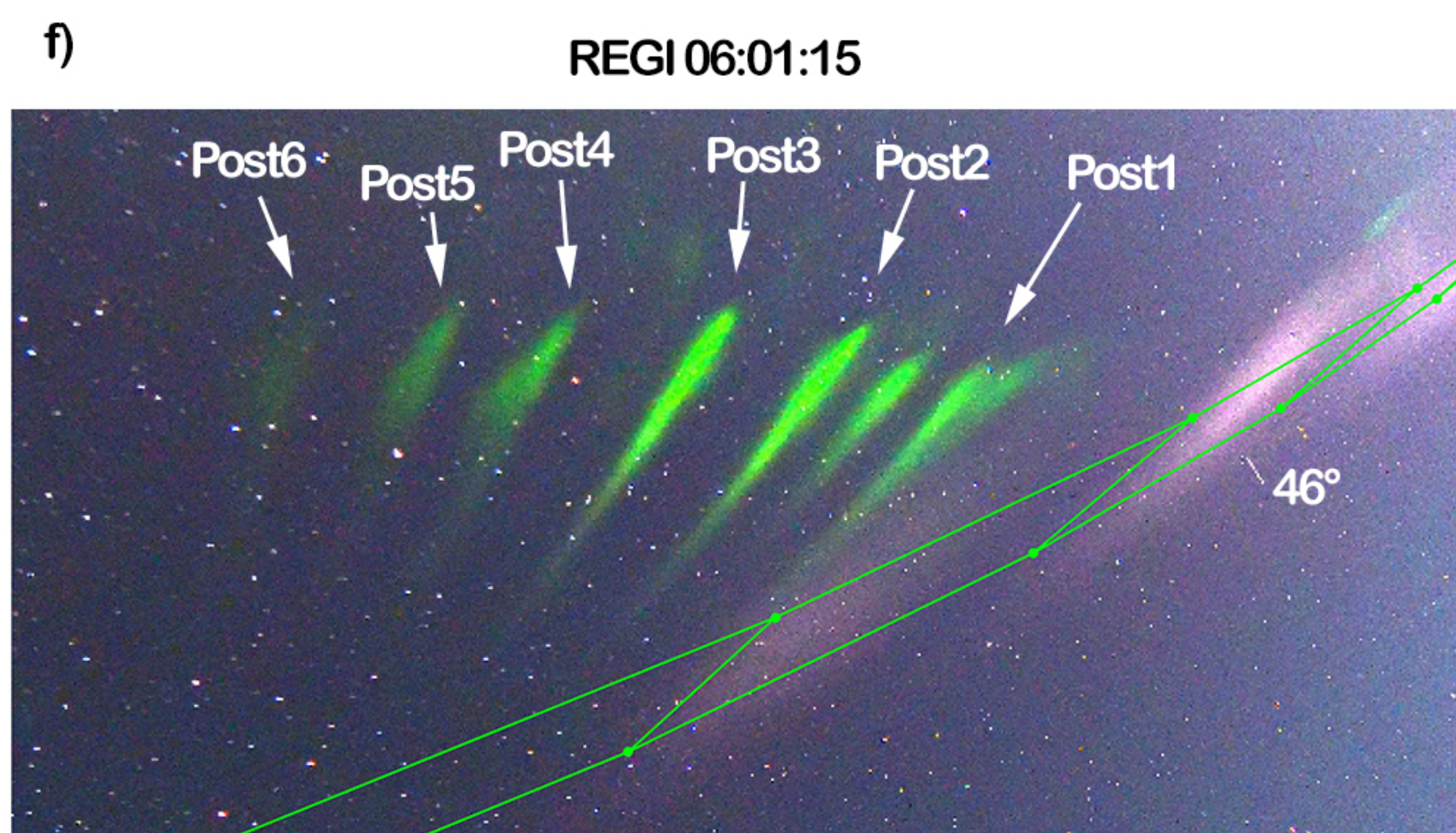
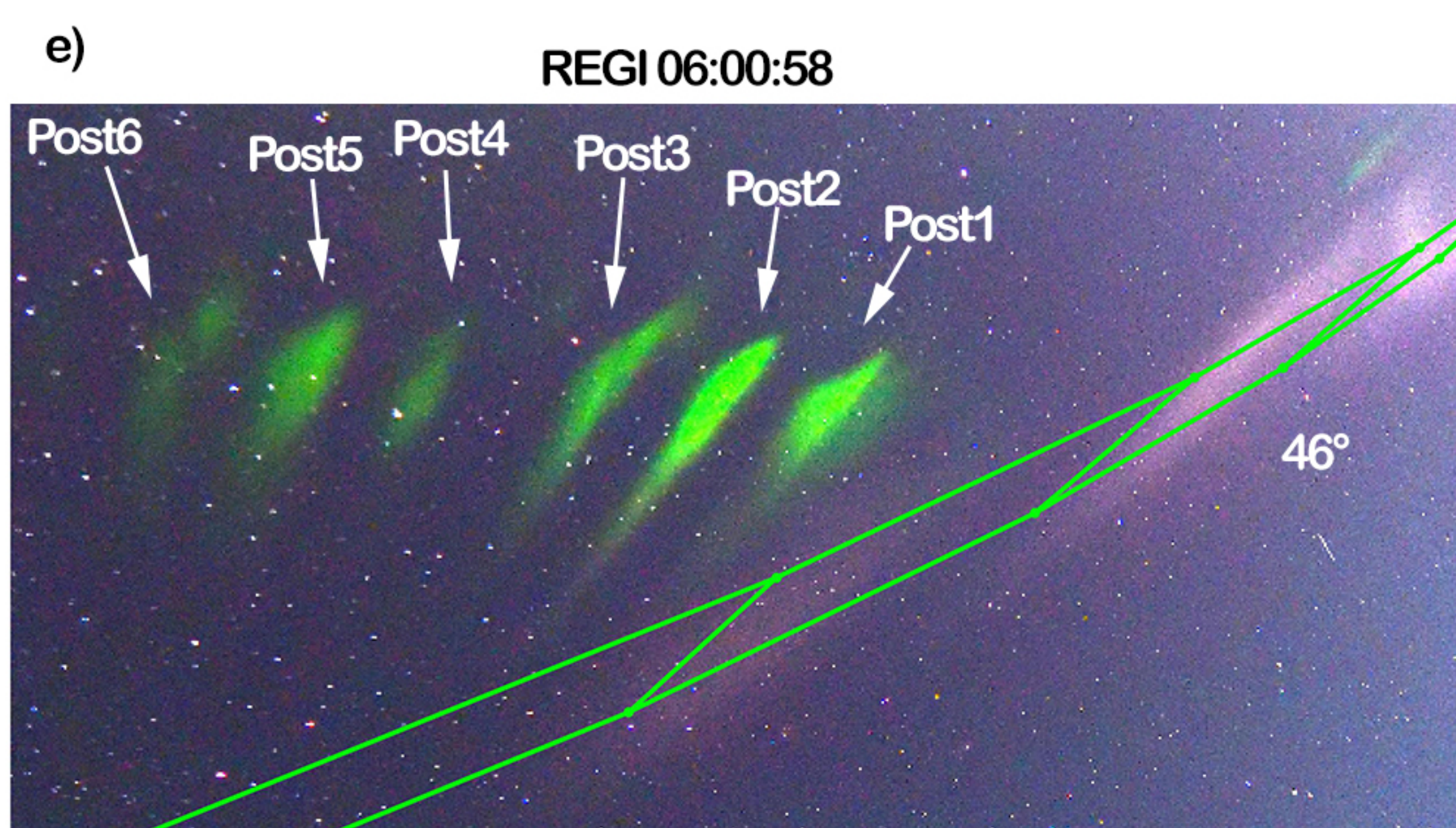
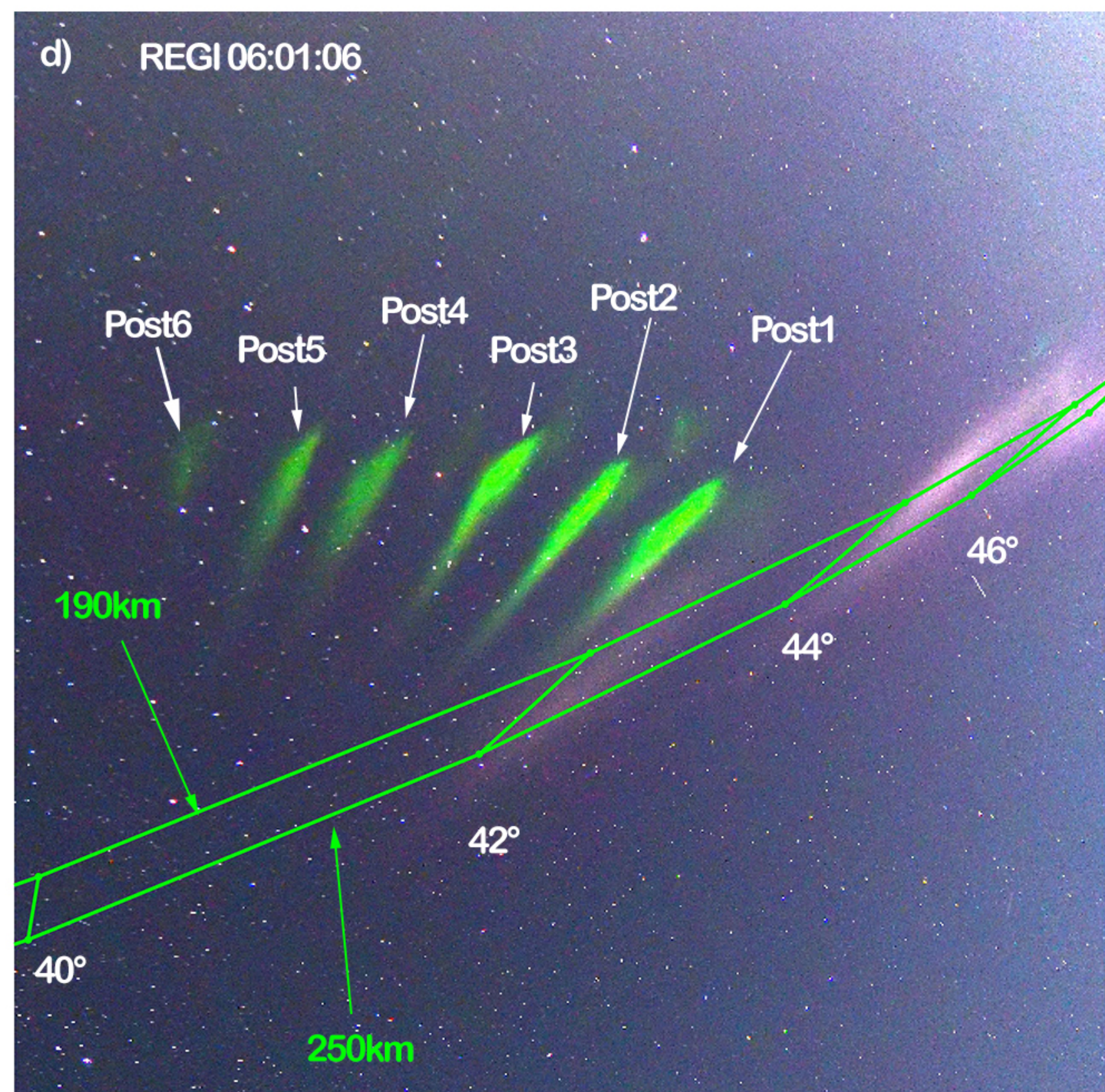
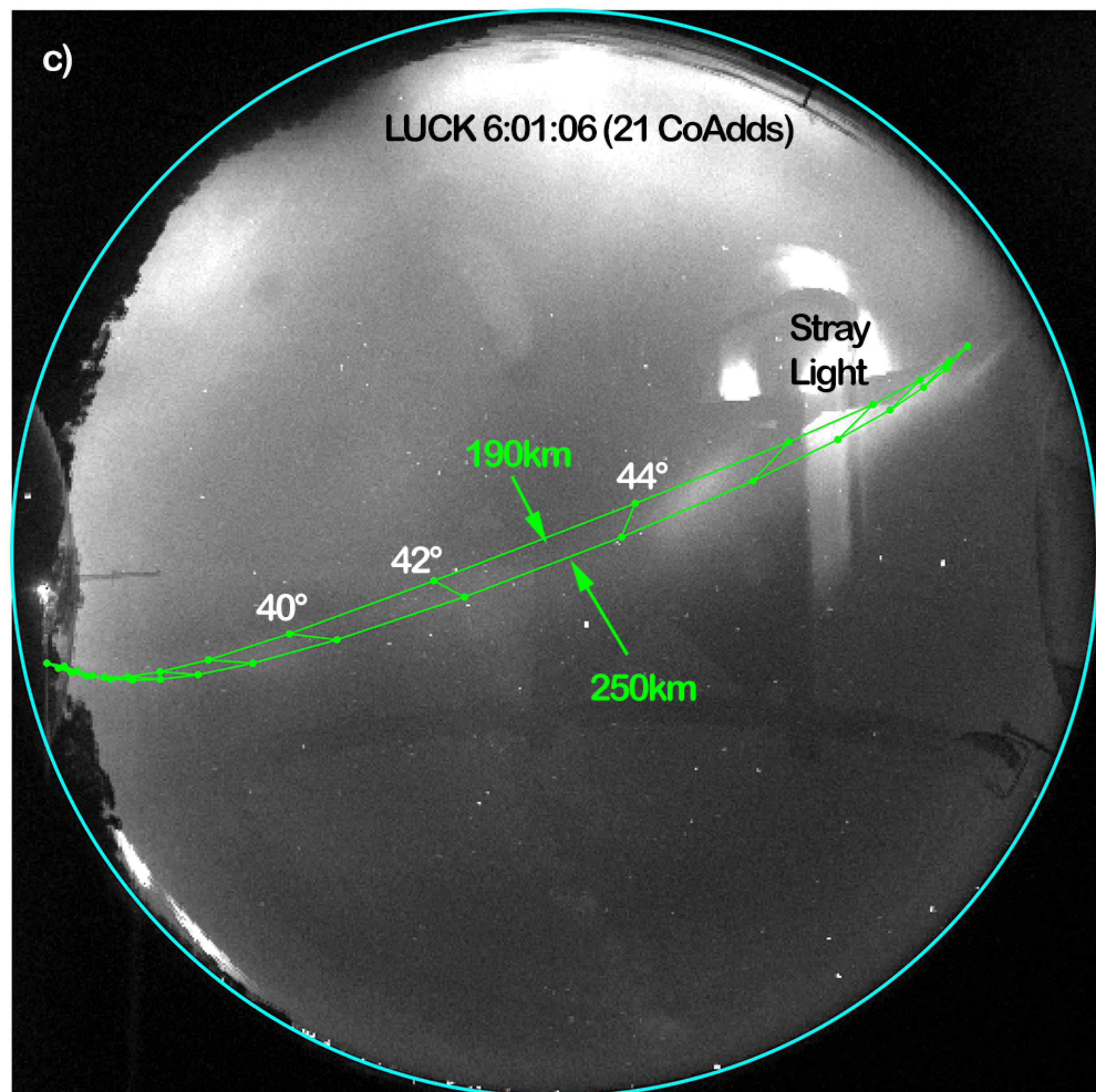
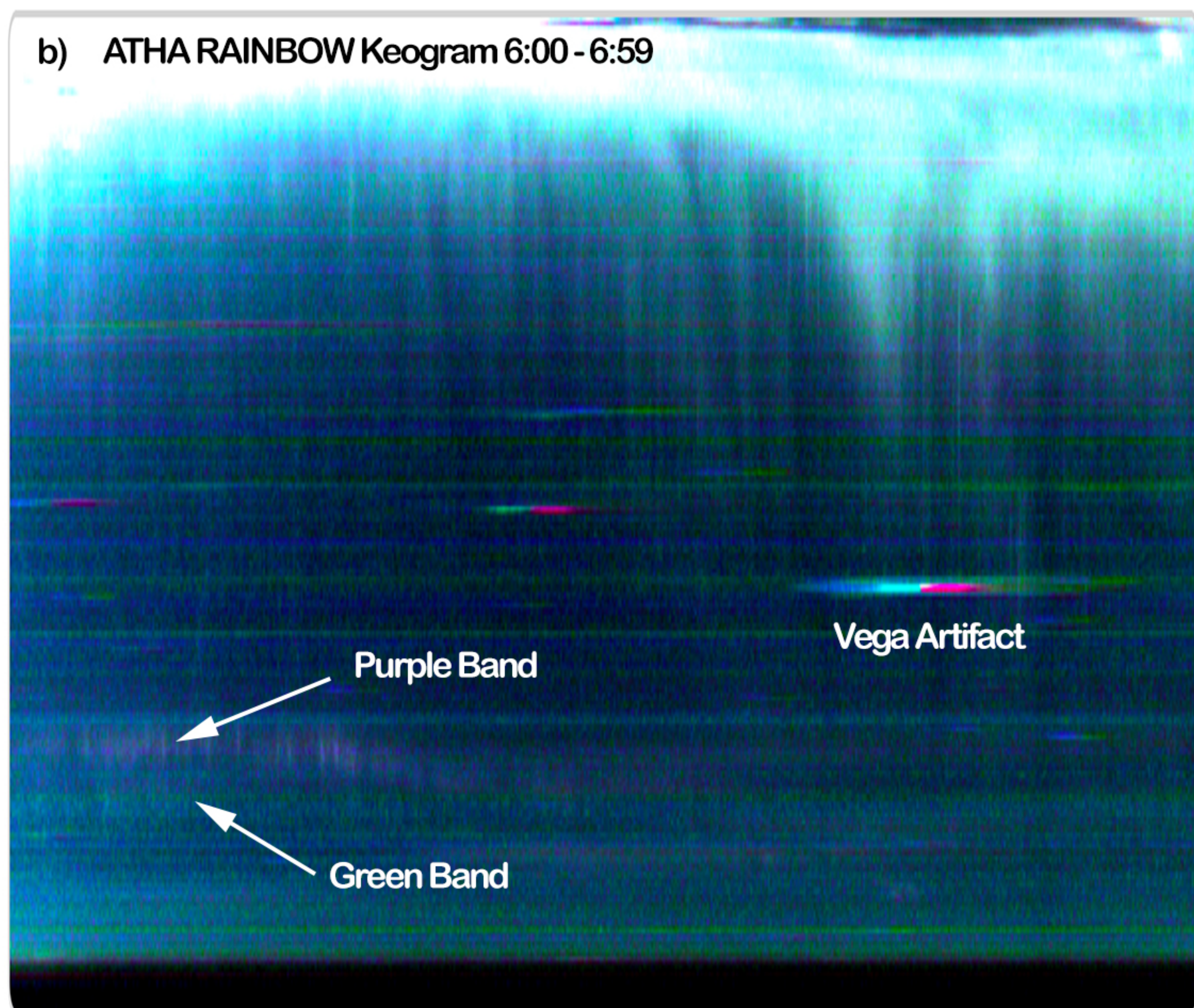
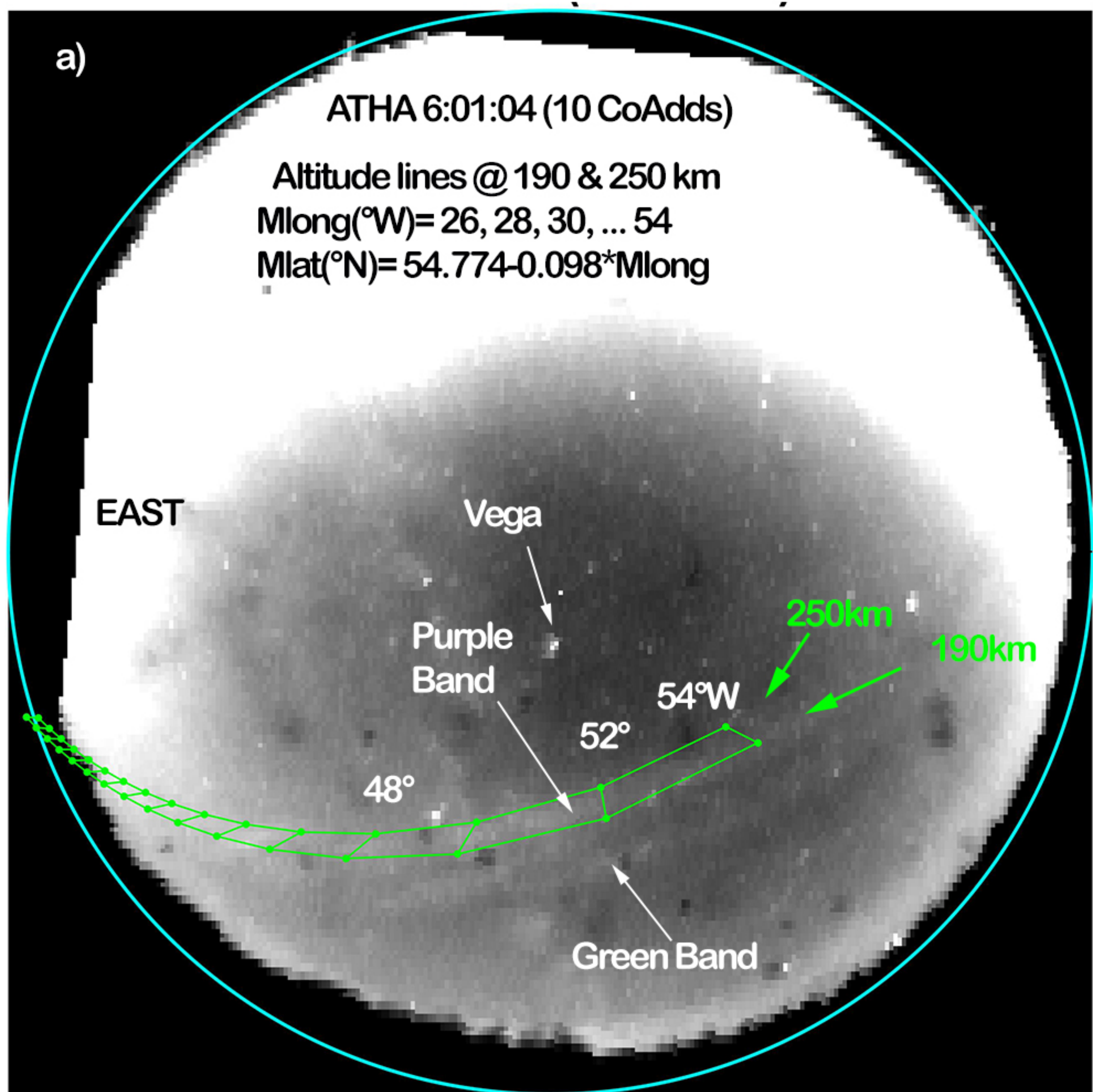


Figure 5.

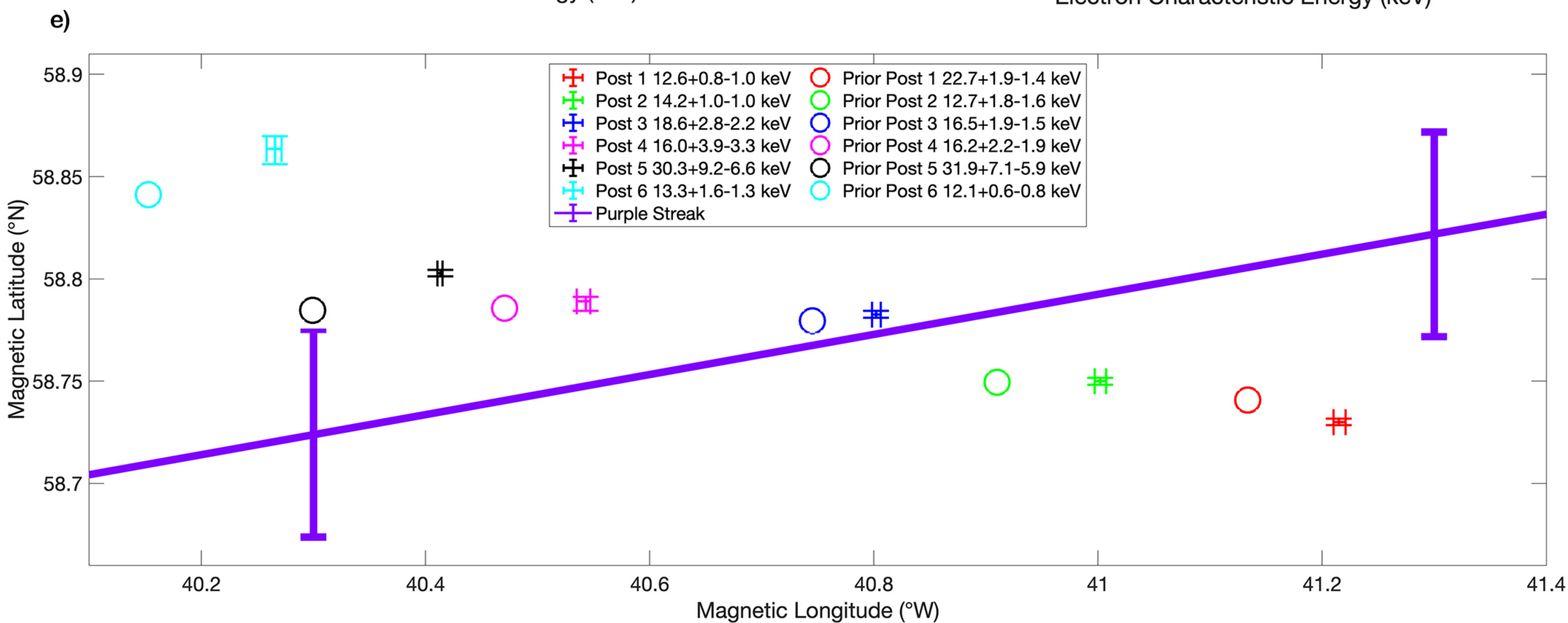
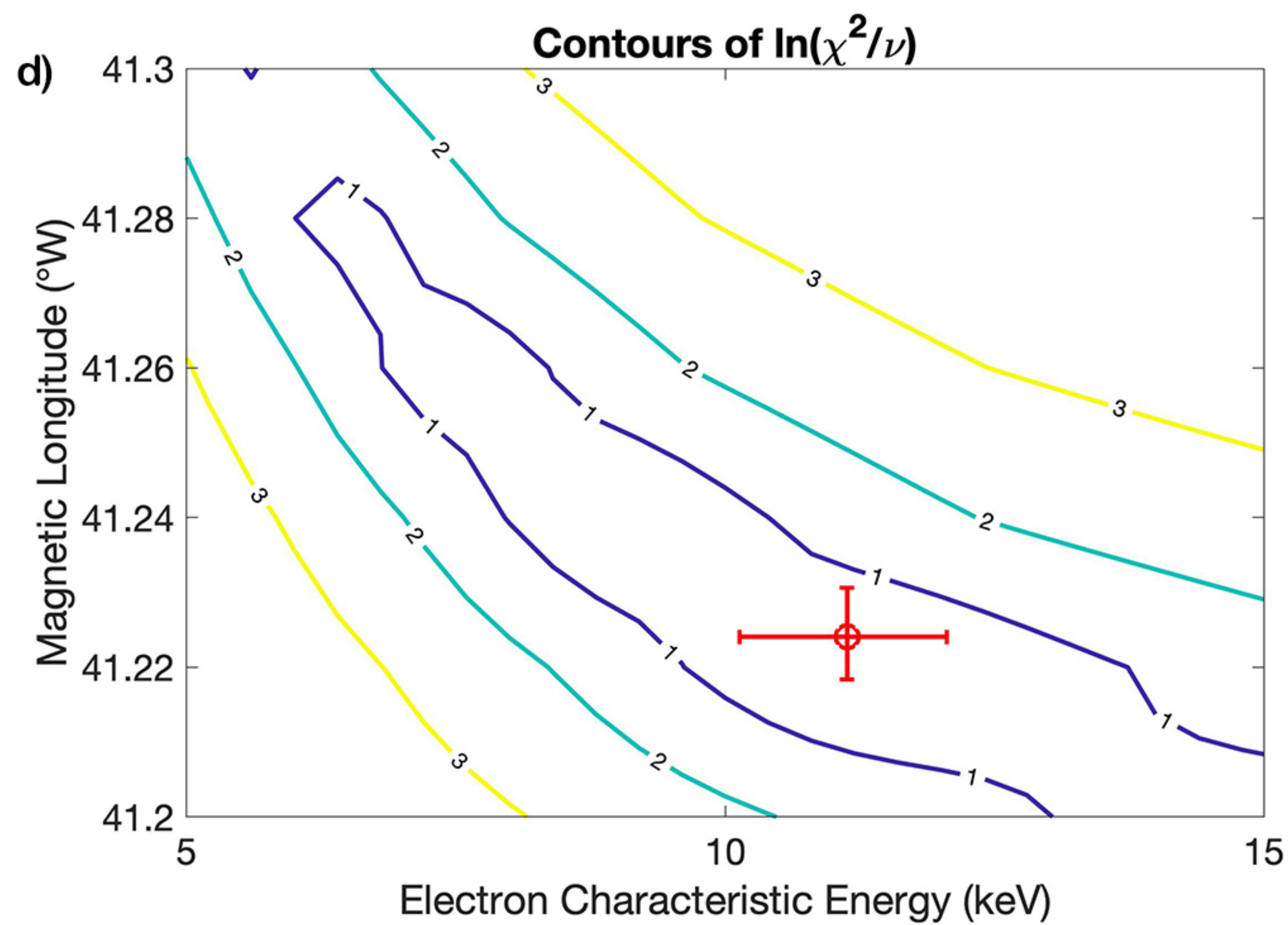
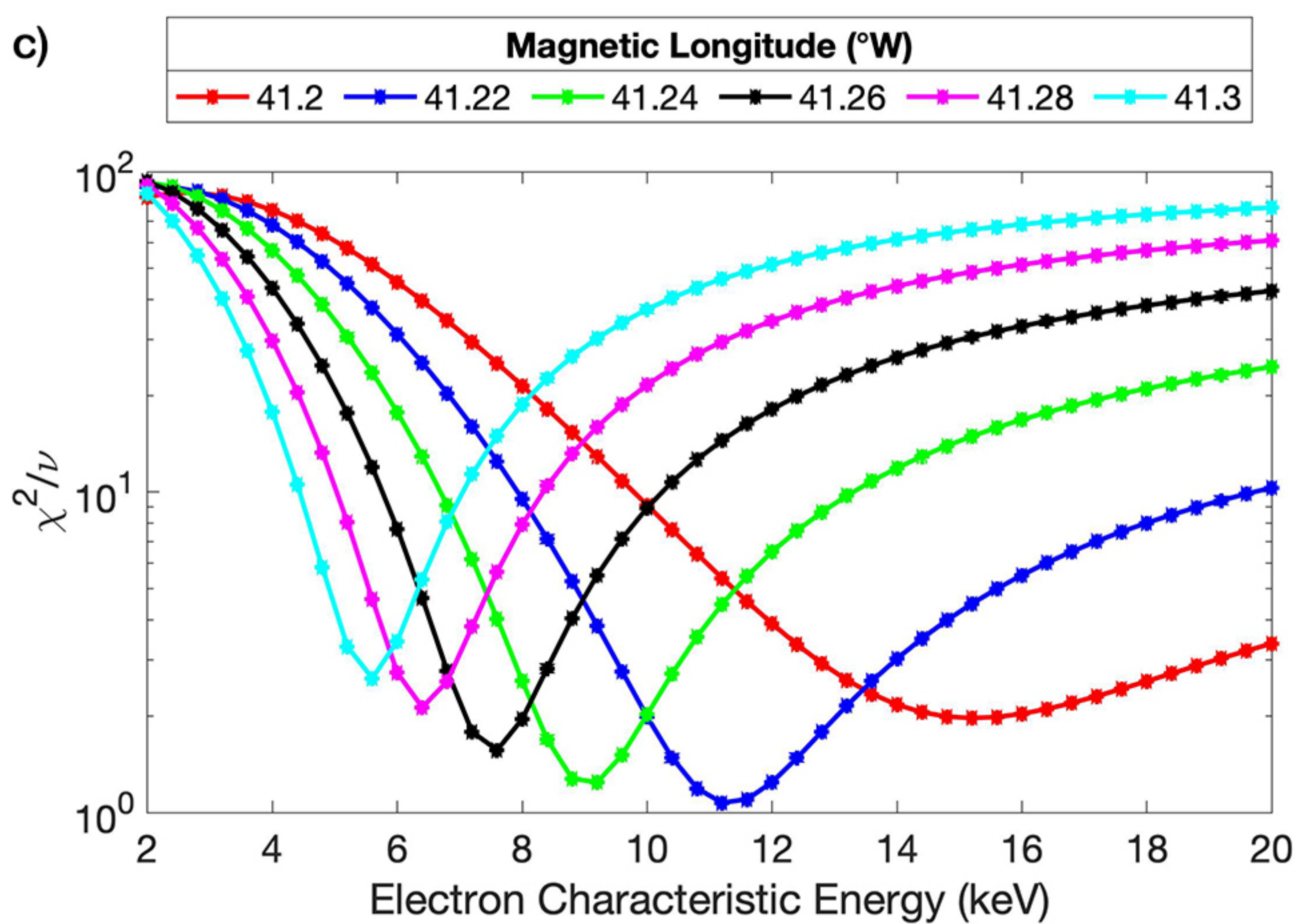
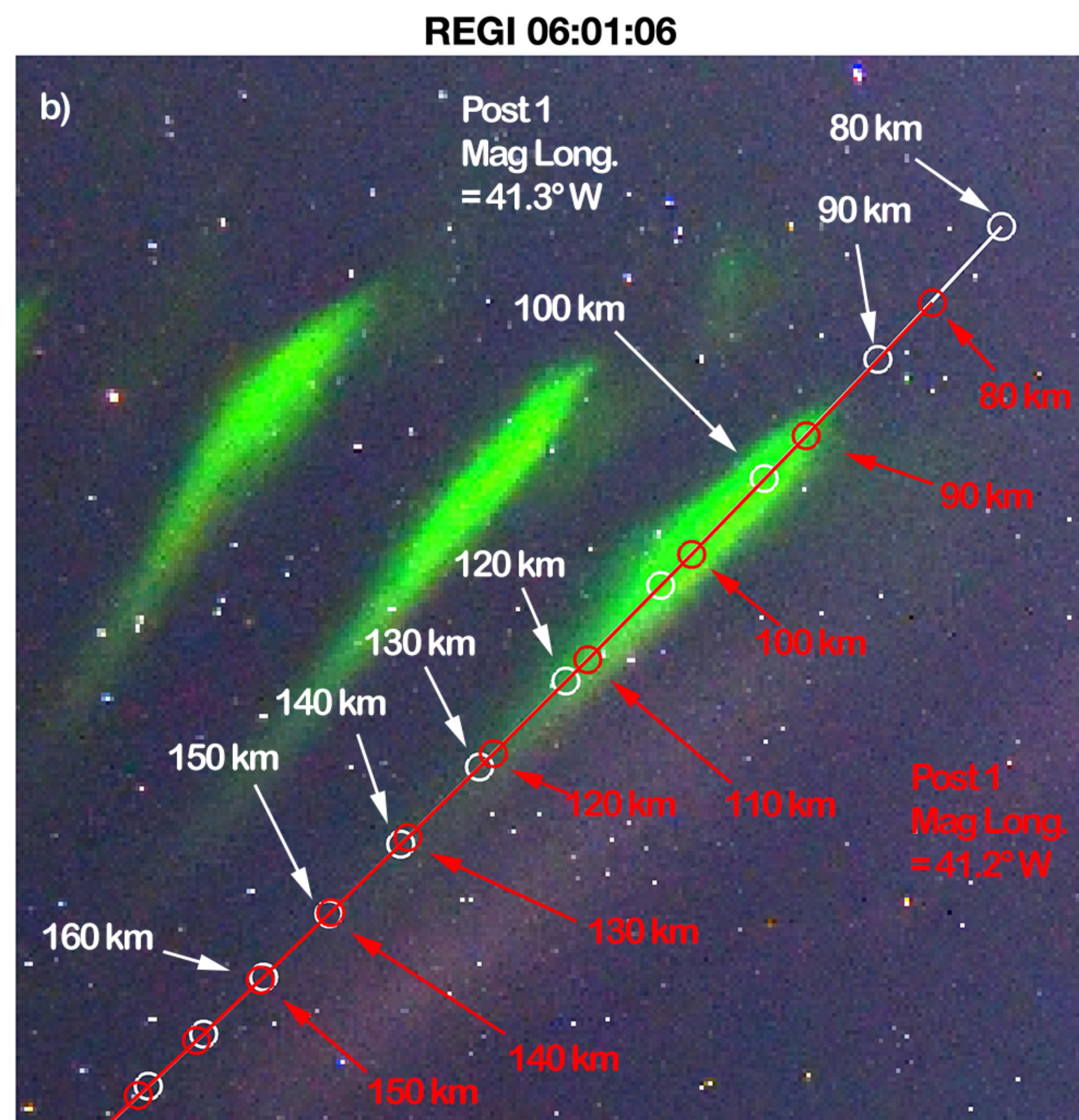
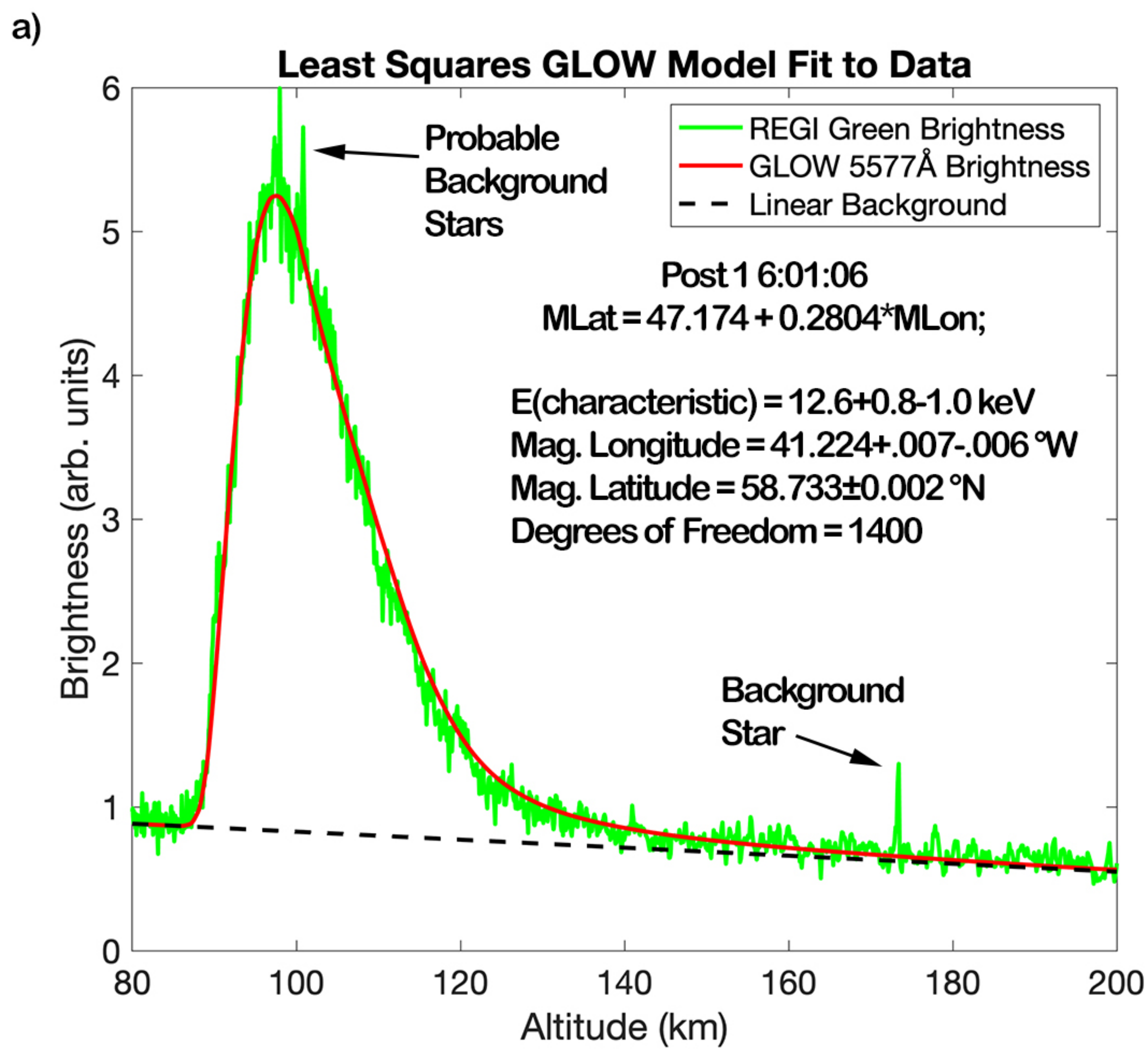


Figure 6.

